This is a repository copy of *Spin-States of Diastereomeric Iron(II) Complexes of 2,6-Bis(thiazolin2-yl)pyridine (ThioPyBox) Ligands and a Comparison with the Corresponding PyBox Derivatives*.

White Rose Research Online URL for this paper:
https://eprints.whiterose.ac.uk/177659/

Version: Accepted Version

Article:

Shahid, N orcid.org/0000-0002-8090-7619, Burrows, KE orcid.org/0000-0002-5485-6256, Howard, MJ orcid.org/0000-0002-0762-2887 et al. (4 more authors) (2021) Spin-States of Diastereomeric Iron(II) Complexes of 2,6-Bis(thiazolin2-yl)pyridine (ThioPyBox) Ligands and a Comparison with the Corresponding PyBox Derivatives. Inorganic Chemistry. ISSN 0020-1669

https://doi.org/10.1021/acs.inorgchem.1c01988

© 2021 American Chemical Society. This document is the Accepted Manuscript version of a Published Work that appeared in final form in Inorganic Chemistry, copyright © American Chemical Society after peer review and technical editing by the publisher. To access the final edited and published work see https://doi.org/10.1021/acs.inorgchem.1c01988. Uploaded in accordance with the publisher's self-archiving policy.

Reuse

Items deposited in White Rose Research Online are protected by copyright, with all rights reserved unless indicated otherwise. They may be downloaded and/or printed for private study, or other acts as permitted by national copyright laws. The publisher or other rights holders may allow further reproduction and re-use of the full text version. This is indicated by the licence information on the White Rose Research Online record for the item.

Takedown

If you consider content in White Rose Research Online to be in breach of UK law, please notify us by emailing eprints@whiterose.ac.uk including the URL of the record and the reason for the withdrawal request.

eprints@whiterose.ac.uk
https://eprints.whiterose.ac.uk/

The Spin States of Diastereomeric Iron(II) Complexes of 2,6-*Bis*(thiazolin-2-yl)pyridine (ThioPyBox) Ligands, and a Comparison with the Corresponding PyBox Derivatives

Namrah Shahid,[†,||] Kay E. Burrows,[†,¶] Mark J. Howard,[†] Christopher M. Pask,[†] Oscar Cespedes,[‡] Patrick C. McGowan[†] and Malcolm A. Halcrow*[,†].

† School of Chemistry, University of Leeds, Woodhouse Lane, Leeds LS2 9JT, U.K.

‡ School of Physics and Astronomy, University of Leeds, EC Stoner Building, Leeds LS2 9JT, U.K.

ABSTRACT: This report investigates homoleptic iron(II) complexes of thiazolinyl analogues of chiral PyBox tridentate ligands: 2,6-*bis*(4-phenyl-4,5-dihydrothiazol-2-yl)pyridine (L^1Ph), 2,6-*bis*(4-*iso*propyl-4,5-dihydrothiazol-2-yl)pyridine (L^1*i*Pr) and 2,6-*bis*(4-*tert*butyl-4,5-dihydrothiazol-2-yl)pyridine (L^1*t*Bu). Crystallographic data imply the larger and more flexible thiazolinyl rings reduce steric clashes between the 'R' substituents in homochiral $[Fe((R)\text{-}L^1R)_2]^{2+}$ or $[Fe((S)\text{-}L^1R)_2]^{2+}$ (R = Ph, *i*Pr or *t*Bu), compared to their PyBox (L^2R) analogues. Conversely, the larger heterocyclic S atoms are in close contact with the R substituents in heterochiral $[Fe((R)\text{-}L^1Ph)((S)\text{-}L^1Ph)]^{2+}$, giving it a more sterically hindered ligand environment than in $[Fe((R)\text{-}L^2Ph)((S)\text{-}L^2Ph)]^{2+}$ (L^2Ph = 2,6-*bis*(4-phenyl-4,5-dihydrooxazol-2-yl)pyridine). Preformed $[Fe((R)\text{-}L^1Ph)((S)\text{-}L^1Ph)]^{2+}$ and $[Fe((R)\text{-}L^1iPr)((S)\text{-}L^1iPr)]^{2+}$ do not racemize by ligand redistribution in CD_3CN solution, but homochiral $[Fe(L^1iPr)_2]^{2+}$ and $[Fe(L^1tBu)_2]^{2+}$ both undergo partial ligand displacement in that solvent. Homochiral $[Fe(L^1Ph)_2]^{2+}$ and $[Fe(L^1iPr)_2]^{2+}$ exhibit spin-crossover equilibria in CD_3CN, centered at 344 ±6 and 277 ±1 K respectively, while their heterochiral congeners are essentially low-spin within the liquid range of the solvent. These data imply the diastereomers of $[Fe(L^1Ph)_2]^{2+}$ and $[Fe(L^1iPr)_2]^{2+}$ show a greater difference in their spin state behaviors than was previous found for $[Fe(L^2Ph)_2]^{2+}$. Gas phase DFT calculations (B86PW91/def2-SVP) of the $[Fe(L^1R)_2]^{2+}$ and $[Fe(L^2R)_2]^{2+}$ complexes reproduce most of the observed trends, but overstabilize the high-spin state of SCO-active $[Fe(L^1iPr)_2]^{2+}$ by *ca.*1.5 kcal mol^{-1}. That might reflect the influence of intramolecular dispersion interactions on the spin states of these compounds. Attempts to model this with the dispersion-corrected functionals B97-D2 or PBE-D3 were less successful than our original protocol, confirming that the spin states of sterically hindered molecules are a challenging computational problem.

Introduction

Iron and other base metals are being increasingly investigated as replacements for expensive heavy metals in applications such as light-harvesting dyes[1] and catalysis.[2] Controlling the metal spin state in such compounds is vital for these applications.[3] Extending the charge-separated lifetimes of iron-containing dye molecules requires a strong ligand field, so their high-spin states are energetically inaccessible.[1] Moreover, hydrogenation and other double bond reductions follow a low-spin catalytic pathway,[4] while cross-coupling[5] or oxidation reactions[6] are favored by high-spin catalytic intermediates. Fine-tuning the ligand field in a catalyst can optimise its performance, or allow a less reactive molecule to access new reaction pathways *via* two-state reactivity.[7]

During our investigations of spin-crossover (SCO) complexes and materials,[8] we found SCO compounds to be powerful probes of the relationship between ligand design and metal ion spin states.[3] This yielded new insights into the effect of remote substituents[9-11] and chelate ligand bite angle[12,13] on a complex's ligand field, and also illustrated how this can be perturbed by crystal packing in the solid state.[14] Another goal was a chiral ligand system, to allow optical isomers of a complex to be distinguished by their spin state.[15,16] Our first attempt towards that aim involved homoleptic iron(II) complexes of the chiral 2,6-*bis*(oxazolinyl)pyridine (PyBox) ligand system (L^2R, Chart 1).[17] Homochiral $[Fe((R)\text{-}L^2Ph)_2]^{2+}$ and heterochiral $[Fe((R)\text{-}L^2Ph)((S)\text{-}L^2Ph)]^{2+}$ exhibit SCO with midpoint temperatures ($T_{½}$) of 244 and 278 K respectively, in CD_3CN solution. That is, the high-spin state of the homochiral diastereomer is more stable than for the heterochiral complex.[15,18] That is a consequence of steric repulsion between pairs of phenyl substituents in the homochiral cation, which is not present in the heterochiral isomer. The more flexible high-spin state allows the geometry of the homochiral molecule to deform to relieve that steric clash, and is thus favored in that isomer.[15,19-21]

This comparison was possible because heterochiral *meso*-$[M((R)\text{-}L^2Ph)((S)\text{-}L^2Ph)]^{2+}$ (M = Fe or another 3*d* cation) complexes are stable in solution.[15,22-24] That contrasts with other $[M((R)\text{-}L^2R)((S)\text{-}L^2R)]^{2+}$ (R = Me, Bn or *i*Pr) species, which spontaneously racemize by ligand redistribution reactions under the same conditions.[15,23,24] Intramolecular π-π interactions between the phenyl substituents and pyridyl rings in $[M((R)\text{-}L^2Ph)((S)\text{-}L^2Ph)]^{2+}$ were proposed to contribute to its stability.[24]

Chart 1 The ThioPyBox (*L^1*R) and PyBox (*L^2*R) ligands referred to in this work (R = H, Ph, *i*Pr or *t*Bu).

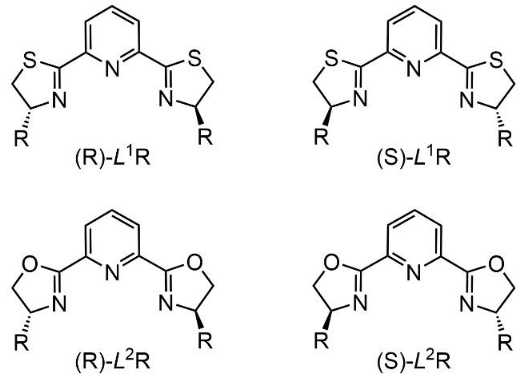

The 34 K difference in $T_{½}$ between the diastereomers of $[Fe(L^2Ph)_2]^{2+}$ corresponds to only 0.3 kJ mol^{-1} in energy terms. In an attempt to amplify the effect, we turned to 2,6-*bis*(thiazolinyl)pyridine (ThioPyBox; L^1R, Chart 1) ligands, whose chemistry is much less developed than their PyBox analogues.[25-31] We reasoned the less electron-withdrawing S heteroatoms in L^1R should make them better σ-donors, thus stabilizing the low-spin state of $[Fe(L^1R)_2]^{2+}$ compared to the corresponding $[Fe(L^2R)_2]^{2+}$ derivatives. Another group recently published $[Fe(L^1H)_2]^{2+}$ and an achiral derivative, showing that assumption is correct.[31] Moreover, the thiazoline rings in L^1R are larger and potentially more flexible than the oxazoline rings in L^2R, which could modify the steric clashes between 'R' substituents in homochiral $[Fe(L^1R)_2]^{2+}$. Thus, a $[Fe(L^1R)_2]^{2+}$ derivative could show the enhanced chiral discrimination of spin-state we are seeking.

We now report the structures and spin state properties of homo- and heterochiral $[Fe(L^1R)_2]^{2+}$ (R = Ph, *i*Pr and *t*Bu), for comparison with their $[Fe(L^2R)_2]^{2+}$ analogues.[18] We also describe the unexpected isolation of $[Fe((S)\text{-}L^2tBu)_2][ClO_4]_2$, the first homoleptic complex of that sterically bulky PyBox derivative.

Experimental

Our synthetic procedure for the L^1R ligands is described in the Supporting Information.[28] Other reagents and solvents were purchased commercially and used as supplied.

CAUTION Although we have experienced no problems when using the perchlorate salts in this study, metal-organic perchlorates are potentially explosive and should be handled with care in small quantities.

Synthesis of the complexes. The following method, described for $[Fe((S)\text{-}L^1Ph)_2][BF_4]_2$, was followed for all the complexes. A solution of (*S*)-L^1Ph (0.060 g, 0.28 mmol) and $Fe[BF_4]_2\cdot 6H_2O$ (0.048 g, 0.14 mmol) in MeCN (5 cm^3) was stirred at room temperature until all the solid had dissolved. Addition of diethyl ether (15 cm^3) to the filtered solution afforded the product as a dark purple powder. Yield 0.067 g, 74 %. Purple single crystals of the complex were grown by slow diffusion of diethyl ether vapor into an acetonitrile solution of the compound.

The same procedure, using equivalent quantities of the appropriate ligand or iron salt, afforded the other complexes in this work.

For $[Fe((S)\text{-}L^1Ph)_2][BF_4]_2$. Purple solid. Elemental analysis for $C_{46}H_{38}B_2F_8FeN_6S_4$ found (calcd) (%) C, 53.4 (53.5), H, 3.68 (3.71), N, 8.18 (8.14). ^{1}H NMR (CD_3CN) δ 3.33, 6.65, 7.98 (all s, 4H, Tz C*H*$_2$ and Ph *H*^{4}), 4.70, 6.23 (both s, 8H, Ph *H*$^{2/6}$ and *H*$^{3/5}$), 9.38 (s, 2H, Py *H*^{4}), 10.84, 14.19 (both s, 4H, Py *H*$^{3/5}$ and Tz C*H*) ppm.

For $[Fe((R)\text{-}L^1Ph)_2][ClO_4]_2$. Purple solid. Elemental analysis for $C_{46}H_{38}Cl_2FeN_6O_8S_4$ found (calcd) (%) C, 52.3 (52.2); H, 3.70 (3.62); N, 8.03 (7.94).

For $[Fe((S)\text{-}L^1Ph)_2][ClO_4]_2$. Purple solid. Elemental analysis for $C_{46}H_{38}Cl_2FeN_6O_8S_4$ found (calcd) (%) 52.3 (52.2), H, 3.70 (3.62), N, 8.03 (7.94). ESMS *m*/*z* 429.0586 (calcd for $[Fe(L^1Ph)_2]^{2+}$ 429.0695), 957.0590 (calcd for $[Fe(L^1Ph)_2(ClO_4)]^+$ 957.0875).

For $[Fe((R)\text{-}L^1Ph)((S)\text{-}L^1Ph)][BF_4]_2$. Purple solid. Elemental analysis for $C_{46}H_{38}B_2F_8FeN_6S_4$ found (calcd) (%) C, 53.4 (53.5), H, 3.76 (3.71), N, 8.25 (8.14) %. ^{1}H NMR (CD_3CN) δ 3.46, 4.13, 4.18 (all m, 4H, Tz C*H* and Tz C*H*$_2$), 6.47 (br s, 8H, Ph *H*$^{3/5}$), 7.18 (t, 8H, Ph *H*$^{2/6}$), 7.29 (s, 4H, Ph *H*^{4}), 8.67 (t, 7.6 Hz, 2H, Py *H*^{4}), 9.09 (br s, 4H, Py *H*$^{3/5}$) ppm.

For $[Fe((R)\text{-}L^1Ph)((S)\text{-}L^1Ph)][ClO_4]_2$. Purple solid. Elemental analysis for $C_{46}H_{38}Cl_2FeN_6O_8S_4$ found (calcd) (%) C, 52.3 (52.2), H, 3.71 (3.62), N, 7.99 (7.94) %. ESMS *m*/*z* 429.0584 (calcd for $[Fe(L^1Ph)_2]^{2+}$ 429.0695), 957.0588 (calcd for $[Fe(L^1Ph)_2(ClO_4)]^+$ 957.0875).

For $[Fe((R)\text{-}L^1iPr)_2][ClO_4]_2$. Purple microcrystals. Elemental analysis for $C_{34}H_{46}Cl_2FeN_6O_8S_4$ found (calcd) (%) C, 44.1 (44.3), H, 4.98 (5.03), N, 8.73 (9.12) %.

For $[Fe((S)\text{-}L^1iPr)_2][ClO_4]_2$. Purple solid. Elemental analysis for $C_{34}H_{46}Cl_2FeN_6O_8S_4$ found (calcd) (%) C, 44.1 (44.3), H, 5.00 (5.03), N, 8.79 (9.12) %. ^{1}H NMR (CD_3CN) δ −17.7 (12H, *i*Pr C*H*$_3$), −11.3 (4H, *i*Pr C*H*), −2.4 (12H, *i*Pr C*H*$_3$), 16.1 (2H, Py *H*^{4}), 20.7, 24.3 (both 4H, Tz C*H*$_2$), 41.5 (4H, Py *H*$^{3/5}$), 49.6 (4H, Tz C*H*) ppm. The solution also contains a second species with resolved peaks at −7.5, −5.2, 11.6 and 54.3 ppm, corresponding to 10 % of the sample; and, a similar quantity of uncoordinated (*S*)-L^1iPr.

For $[Fe((R)\text{-}L^1iPr)((S)\text{-}L^1iPr)][ClO_4]_2$. Purple solid. Elemental analysis for $C_{34}H_{46}Cl_2FeN_6O_8S_4$ found (calcd) (%) C, 44.4 (44.3), H, 4.76 (5.03), N, 8.99 (9.12) %. ^{1}H NMR (CD_3CN) δ 0.00 (s, 12H, *i*Pr C*H*$_3$), 0.21 (s, 4H, *i*Pr C*H*), 0.50 (s, 12H, *i*Pr C*H*$_3$), 3.87, 4.08 (both s, 4H, Tz C*H*$_2$), 4.98 (d, 4H, Tz C*H*), 9.84 (s, 2H, Py *H*^{4}), 13.35 (s, 4H, Py *H*$^{3/5}$) ppm.

For $[Fe((S)\text{-}L^1tBu)_2][ClO_4]_2$. Red solid. Elemental analysis for $C_{38}H_{54}Cl_2FeN_6O_8S_4\cdot 1.5H_2O$ found (calcd) (%) C, 45.3 (45.4), H, 5.30 (5.72), N, 8.14 (8.36). ^{1}H NMR (CD_3CN) δ −22.3 (36H, *t*Bu C*H*$_3$), 16.3 (2H, Py *H*^{4}), 41.9, 52.3, 54.8 (all 4H, Py *H*$^{3/5}$ and Tz C*H*$_2$), 96.8 (4H, Tz C*H*) ppm. The solution also contains a second species with resolved peaks at −11.4, 25.2, 27.3 and 57.6 ppm, corresponding to 19 % of the sample; and, a similar quantity of uncoordinated (*S*)-L^1tBu.

For $[Fe((S)\text{-}L^2tBu)_2][ClO_4]_2$. Red solid. Elemental analysis for $C_{38}H_{54}Cl_2FeN_6O_{12}$ found (calcd) (%) C, 49.9 (50.0), H, 6.14 (5.96), N, 9.04 (9.20). ^{1}H NMR (CD_3CN) δ −16.7 (36H, *t*Bu C*H*$_3$), 23.3 (2H, Py *H*^{4}), 28.5, 38.2 (both 4H, Ox C*H*$_2$), 57.4 (4H, Py *H*$^{3/5}$), 79.2 (4H, Ox C*H*) ppm.

Single Crystal Structure Analyses

Diffraction data for $(R)\text{-}L^1t\mathrm{Bu}$, $[\mathrm{Fe}((S)\text{-}L^1\mathrm{Ph})_2][\mathrm{BF}_4]_2\cdot\mathrm{MeCN}$, $[\mathrm{Fe}((R)\text{-}L^1\mathrm{Ph})((S)\text{-}L^1\mathrm{Ph})][\mathrm{BF}_4]_2\cdot 3/2\mathrm{MeCN}$ and $[\mathrm{Fe}((S)\text{-}L^1t\mathrm{Bu})_2][\mathrm{ClO}_4]_2\cdot\mathrm{Me_2CO}$ were recorded at station I19 of the Diamond synchrotron (λ = 0.6889 Å). Other crystallographic data were measured with an Agilent Supernova diffractometer using monochromated Cu-K_α (λ = 1.5418 Å) radiation and an Oxford Cryostream cryostat. All the structures were solved by direct methods (*SHELXS97*[32]), and developed by full least-squares refinement on F^2 (*SHELXL-2018*[32]). Crystallographic figures were prepared using *XSEED*,[33] and octahedral coordination volumes (V_{Oh}) were calculated with *Olex2*.[34] Experimental details (Tables S1 and S2) and refinement procedures for the structure determinations are given in the Supporting Information.

Other measurements

Elemental microanalyses were performed at the London Metropolitan University School of Human Sciences. Electrospray mass spectra were recorded on a Bruker Micro-TOF-q instrument, from chloroform (organic compounds) or acetonitrile solution (metal complexes). Sodium-containing species in the mass spectra originate from the sodium formate calibrant used. Diamagnetic NMR spectra employed a Bruker AV3HD spectrometer operating at 400.1 (^{1}H) or 100.6 MHz (^{13}C); or, a JEOL ECA600ii spectrometer operating at 600.1 (^{1}H) or 150.9 MHz (^{13}C). Paramagnetic ^{1}H NMR spectra were obtained with a Bruker AV3 spectrometer operating at 300.1 MHz.

The complex solvate crystals gradually lose solvent on exposure to air, and gave ambiguous microanalyses. So, to avoid uncertainty about sample composition, solid state magnetic measurements and powder diffraction patterns were obtained from dried, analytically pure materials. X-ray powder diffraction data were measured using a Bruker D2 Phaser diffractometer. Solid state magnetic susceptibility data were obtained on a Quantum Design MPMS-3 VSM magnetometer, with an applied field of 5000 G and a scan rate of 5 K min^{-1}. A diamagnetic correction for the sample was estimated from Pascal's constants;[35] a diamagnetic correction for the sample holder was measured separately.

Evans method solution magnetic measurements were performed on a Bruker AV-NEO spectrometer operating at 500.2 MHz (^{1}H), or the JEOL ECA600ii spectrometer.[36] Corrections for the diamagnetism of the sample,[35] and the variation of the solvent density with temperature,[37] were applied to the data. The parameters in Table 2 were derived by fitting these data to eq (1) and (2):[38]

$$\ln[(1 - n_{\mathrm{HS}}(T))/\ n_{\mathrm{HS}}(T)] = \Delta H/\ RT - \Delta S/\ R \qquad (1)$$

$$\Delta S = \Delta H/\ T_{1/2} \qquad (2)$$

DFT calculations were performed using *SPARTAN'18* for Windows,[39] with the B86PW91, B97-D2 or PBE-D3 functionals and the def2-SVP basis set. Low-spin systems were treated as spin-restricted, and high-spin systems were treated as spin-unrestricted. The calculations were performed in the gas phase, since a solvent gradient for iron is not implemented in *SPARTAN'18*. The molecules were constructed *de novo* in the program, then subjected to a preliminary molecular mechanics minimization before the full DFT energy minimization was undertaken. Homochiral complexes were calculated as their (R) isomers.

Results and Discussion

Synthesis and Crystallography

Several synthetic procedures for ThioPyBox derivatives have been reported.[25-31] They are usually prepared from pyridine-2,6-dicarbonyl dichloride in two steps: *bis*-amidation with a chiral 2-hydroxyethylamine; then thiolation and ring cyclization of the pyridine-2,6-di(2-hydroxyethylamide) intermediate, using $\mathrm{P_2S_5}$[28,30,31] or Lawesson's reagent[27] under basic conditions. The latter step usually gives moderate yields (30-50 %), and requires significant purification to remove excess sulfur reagents and byproducts. In our hands, Lawesson's reagent gave the best yields of L^1Ph, L^1iPr and L^1tBu (Chart 1). The identities of $(S)\text{-}L^1i\mathrm{Pr}$, $(R)\text{-}L^1t\mathrm{Bu}$ and $(S)\text{-}L^1t\mathrm{Bu}$ were confirmed crystallographically, while a racemic conglomerate $(R)\text{-}L^1t\mathrm{Bu}\cdot(S)\text{-}L^1t\mathrm{Bu}$ was also crystallized during this work (Figures S4-S9).

The homochiral and heterochiral diastereomers of $[\mathrm{Fe}(L^1\mathrm{Ph})_2]^{2+}$ and $[\mathrm{Fe}(L^1i\mathrm{Pr})_2]^{2+}$, and homochiral $[\mathrm{Fe}(L^1t\mathrm{Bu})_2]^{2+}$ and $[\mathrm{Fe}(L^2t\mathrm{Bu})_2]^{2+}$, were prepared by complexing iron(II) salts with the appropriate combination of ligands. The complexes were investigated as their $\mathrm{BF_4}^-$ or $\mathrm{ClO_4}^-$ salts, depending on which anion afforded the best crystals for crystallographic study. Attempts to isolate heterochiral $[\mathrm{Fe}((R)\text{-}L^1t\mathrm{Bu})((S)\text{-}L^1t\mathrm{Bu})][\mathrm{ClO}_4]_2$ were unsuccessful, as described below.

Salts of homochiral $[\mathrm{Fe}(L^1\mathrm{Ph})_2]^{2+}$ crystallize well. Structures were obtained of isomorphous $[\mathrm{Fe}((S)\text{-}L^1\mathrm{Ph})_2][\mathrm{BF}_4]_2\cdot\mathrm{MeCN}$, and both homochiral enantiomers of $[\mathrm{Fe}(L^1\mathrm{Ph})_2][\mathrm{ClO}_4]_2\cdot\mathrm{MeCN}$ (all space group $P2_12_12_1$ with Z = 4). An attempt to prepare $[\mathrm{FeCl_2}((R)\text{-}L^1\mathrm{Ph})]$ instead afforded crystals of $[\mathrm{Fe}((\mathrm{R})\text{-}L^1\mathrm{Ph})_2][\mathrm{Fe^{III}Cl_4}]_2\cdot\mathrm{Et_2O}$ (also $P2_12_12_1$, Z = 4), although that salt was not isolated as an analytically pure material. This contrasts with previously published $[\mathrm{Fe}((\mathrm{R})\text{-}L^1\mathrm{Ph})_2][\mathrm{Fe^{II}Cl_4}]$, which was also produced by a similar reaction.[28] Two different racemic crystals of this complex were also obtained: the homochiral racemic conglomerate $[\mathrm{Fe}((R)\text{-}L^1\mathrm{Ph})_2][\mathrm{Fe}((S)\text{-}L^1\mathrm{Ph})_2][\mathrm{ClO}_4]_4\cdot 2\mathrm{MeCN}$ ($I\bar{4}$, Z = 8), and the heterochiral complex $[\mathrm{Fe}((R)\text{-}L^1\mathrm{Ph})((S)\text{-}L^1\mathrm{Ph})][\mathrm{BF}_4]_2\cdot 2\mathrm{MeCN}$ ($P\bar{1}$, Z = 4). Our isolation of racemic $[\mathrm{Fe}(L^1\mathrm{Ph})_2]^{2+}$ in both its *rac* homochiral and *meso* heterochiral forms is discussed further below.[18]

All these crystals are low-spin at the temperature of measurement, between 100-150 K (Table S3), and the inner coordination geometry of the $[\mathrm{Fe}(L^1\mathrm{Ph})_2]^{2+}$ cations is mostly consistent in each structure. There is one clear difference between the diastereomers, however, in the dihedral angle between the least squares planes of the heterocyclic cores of the two ligands (θ), which should ideally be 90° (Chart S2).[40] The homochiral $[\mathrm{Fe}(L^1\mathrm{Ph})_2]^{2+}$ structures exhibit $84.33(11) \leq \theta \leq 86.26(3)°$, but $\theta = 88.76(4)\text{-}89.60(4)°$ in the heterochiral diastereomer crystal (Figure 1 and Table S3). The small distortion in the homochiral isomer reflects inter-ligand steric repulsion, between pairs of phenyl groups occupying the same molecular quadrant (Figure 1). The effect seems slightly greater than for homochiral $[\mathrm{Fe}(L^2\mathrm{Ph})_2]^{2+}$, where θ spans a range of 85.36(5)-88.07(5)° in its low-spin crystal structures.[15,20,40]

Comparison of the homochiral structures shows some flexibility in the L^1Ph ligand framework (Figures 1 and S19).

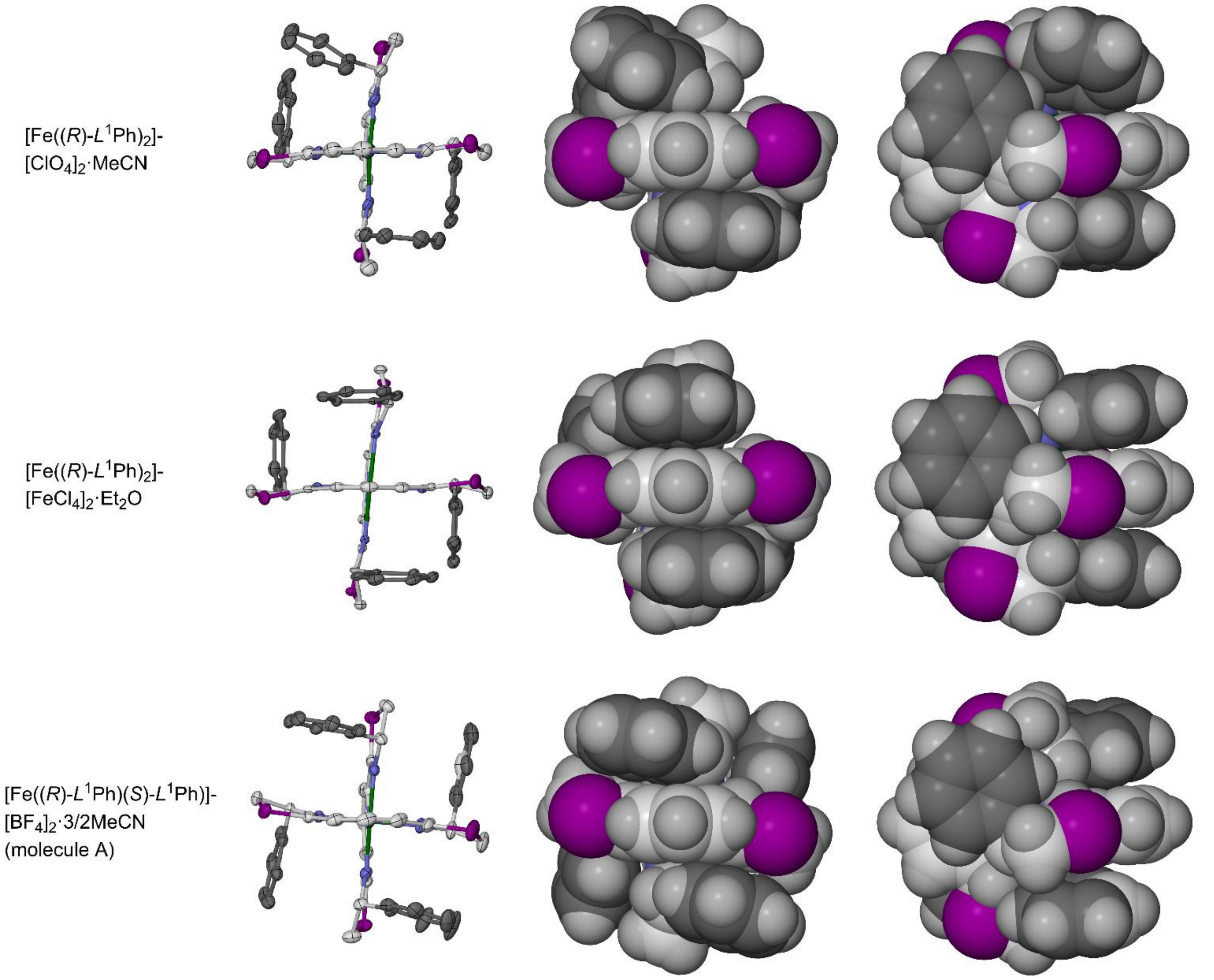

Figure 1 The cations in two crystal forms of homochiral [Fe((*R*)-L^1Ph)$_2$]$^{2+}$ (top and center) and heterochiral *meso*-[Fe((*R*)-L^1Ph)((*S*)-L^1Ph)]$^{2+}$ (bottom). The left-hand views have displacement ellipsoids at the 50% probability level, and H atoms omitted for clarity. The left and center views have the same orientation, whereas the right views are rotated by 90° to highlight steric contacts between ligand substituents. Color code: C{heterocyclic}, white; C{phenyl}, dark gray; H, pale gray; Fe, green; N, blue; S, purple.

The phenyl groups of each L^1Ph ligand in the cation are positioned above and below the pyridyl group of the other ligand. In isostructural homochiral [Fe(L^1Ph)$_2$]X$_2$·MeCN (X$^-$ = BF$_4^-$ or ClO$_4^-$), a steric clash between two phenyl rings leads to one phenyl group being canted with respect to the central pyridyl ring (Figure 1, top). The other phenyl rings in [Fe(L^1Ph)$_2$]X$_2$·MeCN, and both phenyl groups in the other homochiral [Fe(L^1Ph)$_2$]$^{2+}$ crystals, stack more regularly above and below their pyridyl neighbor (Figure 1, center).

The four phenyl groups of heterochiral [Fe((*R*)-L^1Ph)((*S*)-L^1Ph)]$^{2+}$ occupy different molecular quadrants, and are well separated from each other (Figure 1, bottom). These are more offset from the sandwiched pyridyl ring than in the homochiral isomer, and are also significantly canted. That reflects intramolecular contacts between each phenyl ring and a thiazolinyl S atom or CH$_2$ group, which are positioned to deflect the phenyl groups in the observed manner (Figures 1 and S21). The thiazoline rings in the homochiral crystals have different conformations, and are not in contact with the phenyl substituents.

The canting of some phenyl groups in homochiral [Fe(L^1Ph)$_2$]X$_2$·MeCN (X = BF$_4^-$ and ClO$_4^-$) is also found in homochiral [M(L^2Ph)$_2$]$^{2+}$ (M = Fe, Co, Cu or Zn) salts.[15,20-24] However, the ligand conformations in homochiral [Fe(L^1Ph)$_2$]$^{2+}$ are generally more regular than in these L^2Ph complexes (Figure S20, Table S4).[15,20-24] That more regular ligand environment is not reflected in the coordination geometry of homochiral [Fe(L^1Ph)$_2$]$^{2+}$, which is slightly more twisted than for [Fe(L^2Ph)$_2$]$^{2+}$ (see above). Hence, the steric clashes between Ph groups bound to the larger thiazolinyl rings in [Fe(L^1Ph)$_2$]$^{2+}$ have a larger impact on the metal coordination geometry, at least in its low-spin state.

Conversely, the phenyl group orientations in heterochiral [Fe((*R*)-L^1Ph)((*S*)-L^1Ph)][BF$_4$]$_2$·2MeCN are more twisted than in [M((*R*)-L^2Ph)((*S*)-L^2Ph)]$^{2+}$ structures (Figure S22, Table S5).[15,21-24] That is a consequence of the larger thiazolinyl rings in L^1Ph, whose S atoms are in direct contact with the phenyl groups in the heterochiral complex as described above (Figure 1, bottom). Those contacts have no apparent impact on the metal coordination geometry however, which is identical with experimental error in those low-spin iron complexes. These crystallographic similarities and differences between the L^1Ph and L^2Ph complexes are replicated in the computational study described below.

While the homochiral isomer of [Fe(L^1*i*Pr)$_2$]X$_2$ (X = BF_4^- or ClO_4^-) was not structurally characterized, heterochiral *meso*-[Fe((*R*)-L^1*i*Pr)((*S*)-L^1*i*Pr)][ClO$_4$]$_2$·2MeCN was successfully crystallized ($C2/c$, $Z = 4$). Its complex cation has crystallographic C_2 symmetry, and is also low-spin at 125 K (Table S6). The L^1*i*Pr ligands are perpendicular to each other [θ = 87.99(9)°] but have more pronounced S-shaped conformations than in its L^1Ph congener, which gives the molecule a small helicity (Figure 2). That reflects the steric influence of the larger *iso*propyl groups, which are all oriented in the same direction in the molecule.

Crystalline [Fe((*S*)-L^1*t*Bu)$_2$][ClO$_4$]$_2$·Me$_2$CO ($P2_12_12_1$, $Z = 4$) is high-spin at 100 K, reflecting the steric influence of its large *tert*butyl substituents.[3,41] The geometry of high-spin [Fe((*S*)-L^1*t*Bu)$_2$]$^{2+}$ is more distorted than the low-spin complexes, and is highly twisted to accommodate steric clashes between its *tert*butyl groups (Figure 3). This again manifests itself in the θ angle between the tridentate ligands (Chart S2), which is 66.07(8)°.[39] That level of distortion should preclude the compound accessing its low-spin state at low temperatures through thermal SCO.[42] Crystals of [Fe((*S*)-L^2*t*Bu)$_2$][ClO$_4$]$_2$·Me$_2$CO are isomorphous with their L^1*t*Bu analogue, and show a similarly twisted coordination geometry (Figure S24 and Table S7). If the complexes retain this geometry in solution, they should also remain high-spin at all temperatures as is observed (see below).

Attempts to isolate heterochiral [Fe(L^1*t*Bu)$_2$]$^{2+}$ were unsuccessful. One such crystallization yielded the conglomerate crystal (*R*)-L^1*t*Bu·(*S*)-L^1*t*Bu mentioned above. Crystals of a solvate of *rac*-[Fe(L^1*t*Bu)(OH$_2$)(NCMe)$_2$][ClO$_4$]$_2$ ($P\bar{1}$, $Z = 2$). were obtained from another reaction, from acetonitrile solution. That cation is high-spin and six-coordinate, with *trans* MeCN ligands (Figures S27-S28).

Other solid-state characterization

Allowing for small differences due to solvent loss, dried samples of homochiral [Fe(L^1Ph)$_2$]X$_2$ (X$^-$ = BF_4^- and ClO_4^-) appear isomorphous with their solvated crystal phases by powder diffraction (Figure S29). Both compounds are predominantly low-spin at room temperature, as expected from their crystal structures. However, each contains a 10-15 % fraction which remains high-spin on cooling, which may be a consequence of loss of lattice solvent from the predried samples. The materials undergo very similar two-step spin-transitions on heating (Figure 4). The first step has $T_{½}$ = 330±2 K, and corresponds to *ca.* 50 % of the fraction of the material which is low-spin at 300 K.[43] The second step is incomplete at 370 K, the highest temperature accessible with our magnetometer. The high-temperature behavior is reversible on re-cooling, and so is not associated with solvent loss.[44] It was impossible to determine the structural basis of the SCO discontinuity, since crystals of [Fe(L^1Ph)$_2$]X$_2$·MeCN are unstable at these temperatures. However, solvates of

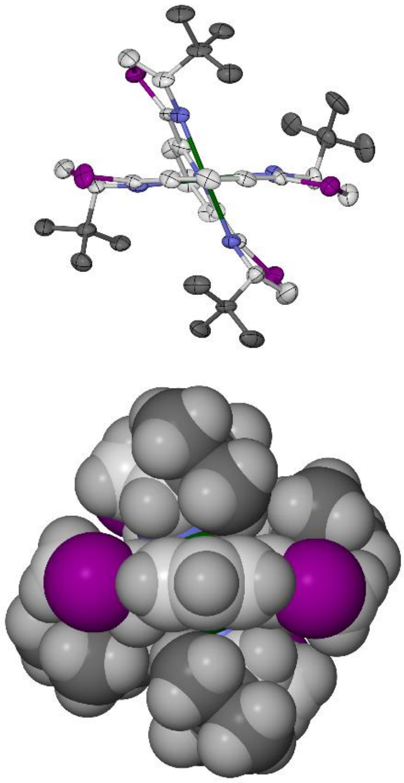

Figure 3 The complex cation in [Fe((*S*)-L^1*t*Bu)$_2$][ClO$_4$]$_2$·Me$_2$CO, showing the steric influence of its *tert*butyl substituents. The images are plotted in the same orientation, along the N{pyridyl}–Fe–N{pyridyl} vector. Other details as for Figure 1.

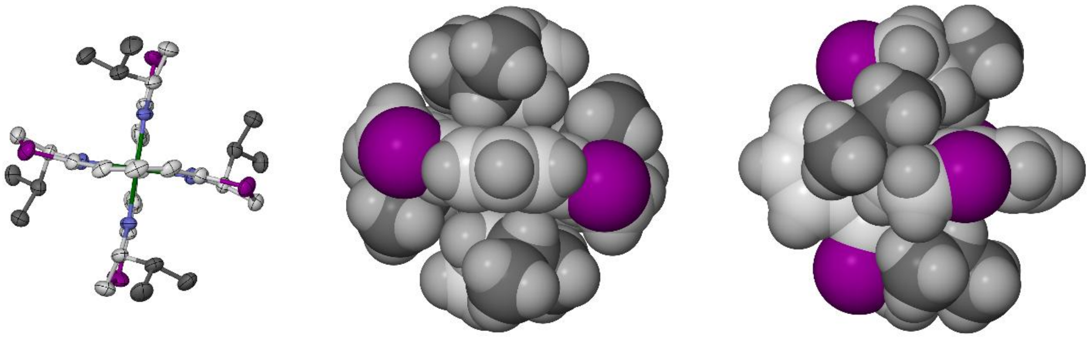

Figure 2 The complex cation in [Fe((*R*)-L^1*i*Pr)((*S*)-L^1*i*Pr)][ClO$_4$]$_2$·2MeCN, showing the steric influence of its *iso*propyl substituents. Details as for Figure 1.

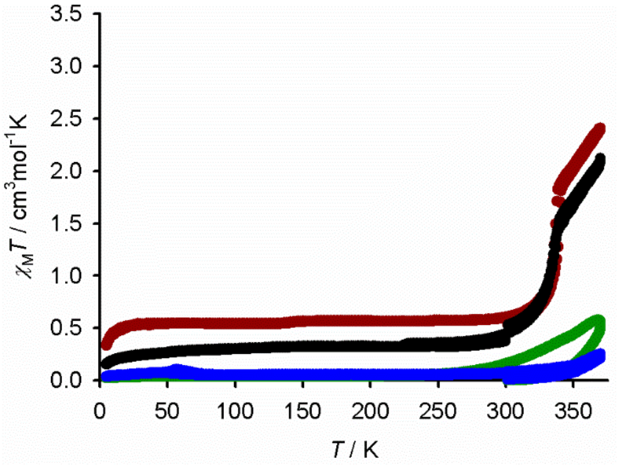

Figure 4 Variable temperature magnetic susceptibility data for homochiral [Fe((*S*)-*L*^{1}Ph)$_2$][BF$_4$]$_2$ (black) and [Fe((*S*)-*L*^{1}Ph)$_2$][ClO$_4$]$_2$ (red), and for heterochiral *meso*-[Fe((*R*)-*L*^{1}Ph)((*S*)-*L*^{1}Ph)][BF$_4$]$_2$ (green) and [Fe((*R*)-*L*^{1}Ph)((*S*)-*L*^{1}Ph)][ClO$_4$]$_2$ (blue). Data were measured in both cooling and warming modes, with a 5 K min^{-1} scan rate.

homochiral [Fe(*L*^{2}Ph)$_2$]X$_2$ exhibit similarly structured SCO below room temperature, reflecting crystallographic phase changes and/or reorientation of their phenyl substituents as the transition proceeds.[15,20]

Recrystallized bulk samples of [Fe((*R*)-*L*^{1}Ph)((*S*)-*L*^{1}Ph)][BF$_4$]$_2$ were phase-pure and isostructural with the crystallized *meso* form of that solvate salt. However, the ClO$_4^-$ salt of the same compound is probably a mixture of its *rac* and *meso* isomers by powder diffraction (Figure S29). Despite their different compositions, both materials are also low-spin but show the onset of gradual thermal SCO above 300 K (Figure 4). The irreversible partial SCO of the BF$_4^-$ salt is intriguing since the sample was solvent-free by microanalysis, but can't be explained without higher temperature data. The solution characterization described below was performed with the isomerically pure BF$_4^-$ salt.

Homochiral [Fe((*S*)-*L*^{1}*i*Pr)$_2$][ClO$_4$]$_2$ is predominantly high-spin at room temperature and exhibits gradual SCO at $T_{½} \approx 215$ K, which is *ca.* 50 % complete at 50 K. Conversely [Fe((*R*)-*L*^{1}*i*Pr)((*S*)-*L*^{1}*i*Pr)][ClO$_4$]$_2$ is low-spin at 300 K but undergoes SCO on warming which is *ca.* 30 % complete at 370 K (Figure S31). Solid [Fe((*S*)-*L*^{1}*t*Bu)$_2$][ClO$_4$]$_2$ and [Fe((*S*)-*L*^{2}*t*Bu)$_2$][ClO$_4$]$_2$ are high-spin between 5-300 K, as predicted from their crystal structures (Figure S32).

Solution properties

The solution speciation of [Fe((*R*)-*L*^{1}Ph)((*S*)-*L*^{1}Ph)]$^{2+}$ resembles the heterochiral [Fe(*L*^{2}Ph)$_2$]$^{2+}$ complex.[15] Thus, freshly prepared CD$_3$CN solutions of a 1:1:1 mixture of (*R*)-*L*^{1}Ph, (*S*)-*L*^{1}Ph and an iron(II) salt contain both the homochiral and *meso*-heterochiral cations in a *ca.* 1:1 ratio by NMR, which does not vary on standing for 2 weeks (Figure S35). Slow crystallization of these solutions with diethyl ether yields the pure *meso*-heterochiral complex as its BF$_4^-$ salt, and a mixture of the *meso*-heterochiral and *rac*-homochiral materials when using Fe[ClO$_4$]$_2$ (Figure S29). We propose the *meso* form has lower solubility and crystallizes preferentially from those solutions as its BF$_4^-$ salt, but the ClO$_4^-$ salts of the two isomers have more similar solubilities. Redissolved samples of pure [Fe((*R*)-*L*^{1}Ph)((*S*)-*L*^{1}Ph)][BF$_4$]$_2$ are stable in solution, showing no racemization by NMR at temperatures up to 348 K, or after standing for 2 weeks at room temperature (Figures S36 and S37).

Preformed [Fe((*R*)-*L*^{1}*i*Pr)((*S*)-*L*^{1}*i*Pr)]$^{2+}$ is also stable in CD$_3$CN (Figure S39). That contrasts with heterochiral [Fe((*R*)-*L*^{2}*i*Pr)((*S*)-*L*^{2}*i*Pr)]$^{2+}$, which forms a mixture of homo- and heterochiral cations by ligand redistribution when redissolved.[15] We attribute that to the predominantly low-spin nature of [Fe((*R*)-*L*^{1}*i*Pr)((*S*)-*L*^{1}*i*Pr)]$^{2+}$ at room temperature (Figure 5), which is inert to ligand exchange reactions. High-spin [Fe((*R*)-*L*^{2}*i*Pr)((*S*)-*L*^{2}*i*Pr)]$^{2+}$ should be more labile to ligand redistribution, as observed.[3]

Partial *L*^{1}R ligand dissociation occurs in CD$_3$CN solutions of [Fe((*S*)-*L*^{1}*i*Pr)$_2$][ClO$_4$]$_2$ and [Fe((*S*)-*L*^{1}*t*Bu)$_2$][ClO$_4$]$_2$. These respectively contain *ca.* 15 % and 25 % of a second paramagnetic species assigned as [Fe(*L*^{1}R)(solv)$_3$]$^{2+}$ (solv = a solvent ligand), and a similar quantity of free *L*^{1}R ligand (Figures S38 and S41). Conversely, there is no detectable ligand dissociation in [Fe((*R*)-*L*^{2}*i*Pr)$_2$][ClO$_4$]$_2$[15] or [Fe((*S*)-*L*^{2}*t*Bu)$_2$][ClO$_4$]$_2$ (Figure S42) in that solvent. That implies the R substituents in [Fe((*S*)-*L*^{1}R)$_2$]$^{2+}$ may have a greater steric influence on the metal coordination sphere than [Fe((*S*)-*L*^{2}R)$_2$]$^{2+}$. Solutions of a 1:1:1 ratio of (*R*)-*L*^{1}*t*Bu, (*S*)-*L*^{1}*t*Bu and Fe[ClO$_4$]$_2$·6H$_2$O in CD$_3$CN contain different proportions of the same species as found for the homochiral complex by ^{1}H NMR (Figure S43). Heterochiral [Fe((*R*)-*L*^{1}*t*Bu)((*S*)-*L*^{1}*t*Bu)$_2$]$^{2+}$ does not appear to exist under these conditions.

Only two of the compounds undergo SCO in solution over the liquid range of CD$_3$CN (Figure 5). Those are: [Fe((*R*)-*L*^{1}Ph)$_2$][ClO$_4$]$_2$, which shows $T_{½} = 344 \pm 6$ K, $\Delta H = 24 \pm 2$ kJ mol^{-1} and $\Delta S = 69 \pm 6$ J mol^{-1} K^{-1}; and, [Fe((*S*)-*L*^{1}*i*Pr)$_2$][ClO$_4$]$_2$ with $T_{½} = 277 \pm 1$ K, $\Delta H = 36 \pm 1$ kJ mol^{-1} and $\Delta S = 129 \pm 6$ J mol^{-1} K^{-1}. The latter data were best fit by a constant residual value of $\chi_M T = 0.5$ cm^3 mol^{-1} K at low temperatures, implying *ca.* 15 % of the sample does not take part in SCO. That is consistent with the fractional *L*^{1}*i*Pr dissociation in

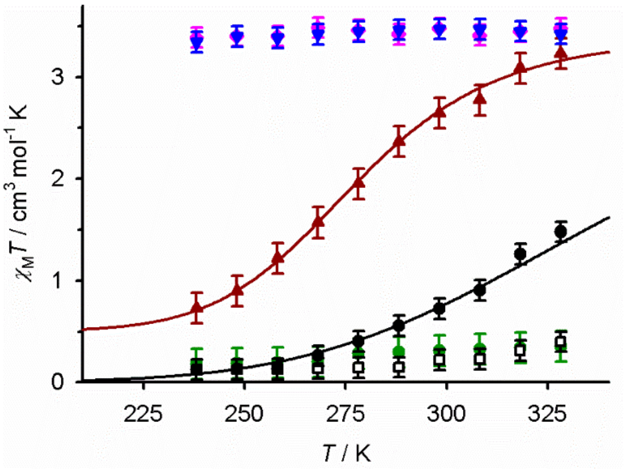

Figure 5 Variable temperature magnetic susceptibility data in CD$_3$CN solution for [Fe((*R*)-*L*^{1}Ph)$_2$][ClO$_4$]$_2$ (black); [Fe((*R*)-*L*^{1}Ph)((*S*)-*L*^{1}Ph)][BF$_4$]$_2$ (white); [Fe((*S*)-*L*^{1}*i*Pr)$_2$][ClO$_4$]$_2$ (red); [Fe((*R*)-*L*^{1}*i*Pr)((*S*)-*L*^{1}*i*Pr)][ClO$_4$]$_2$ (green); [Fe((*S*)-*L*^{1}*t*Bu)$_2$][ClO$_4$]$_2$ (blue); and [Fe((*S*)-*L*^{2}*t*Bu)$_2$][ClO$_4$]$_2$ (pink). The lines show the best fits of the data to eq 1 and 2.

solutions of that complex (Figure S38), and its larger ΔH value which can indicate a ligand exchange pre-equilibrium in the SCO process.[45] The heterochiral isomers of both complexes are low-spin at room temperature, but show a small paramagnetism on warming that may indicate the onset of SCO.[46] $[\mathrm{Fe}((S)\text{-}L^1t\mathrm{Bu})_2][\mathrm{ClO_4}]_2$ and $[\mathrm{Fe}((S)\text{-}L^2t\mathrm{Bu})_2][\mathrm{ClO_4}]_2$ are both high-spin above 248 K.

The spin states of the complexes in solution and the solid state resemble each other well, except for $[\mathrm{Fe}((S)\text{-}L^1i\mathrm{Pr})_2][\mathrm{ClO_4}]_2$ whose partial SCO occurs at *ca.* 100 K lower temperature in the solid state (Figure S33). It's well known that SCO in the solid state can be strongly perturbed by the constraints of the rigid solid lattice, which are not a factor in fluid solution.[14]

The stabilization of the high-spin state in homochiral *vs* heterochiral $[\mathrm{Fe}(L^1\mathrm{R})_2]^{2+}$ (R = Ph or *i*Pr) cannot be quantified from these data, because SCO was not observed in the heterochiral diastereomers. However, after applying eq (1) and (2) to the heterochiral complex data, we estimate $T_{1/2}$ in the homochiral complex is ≥45 K lower than its heterochiral congener for R = Ph, and ≥85 K lower for R = *i*Pr.[45] Both those differences are larger than we previously found for the diastereomers of $[\mathrm{Fe}(L^2\mathrm{Ph})_2]^{2+}$.[15]

DFT calculations

The spin states and stabilities of the diastereomers of $[\mathrm{Fe}(L^1\mathrm{R})_2]^{2+}$ and $[\mathrm{Fe}(L^2\mathrm{R})_2]^{2+}$ were further investigated by gas phase DF calculations. Initial calculations employed the B86PW91 functional and def2-SVP basis set combination, since this and closely related methods perform well in comparative spin state energy calculations in iron(II) complexes of tridentate heterocyclic ligands.[9,12,47-49]

The minimized geometries of the complexes are in generally good agreement with experiment (Tables S10-S11, Figure S48-S56).[50] The 'R' substituents in the homochiral complexes induce twisting of the ligands to relieve intramolecular steric clashes, as in Figure 3. This is reflected in a reduction of θ below its ideal value of 90° (Tables S10 and S11).[40] The distortion increases as R = Ph < *i*Pr < *t*Bu, and is greater in the high-spin molecules as expected.[42] It is also consistently larger in the L^1R complexes than their L^2R analogues, for a given 'R' group. Computed θ values in high-spin $[\mathrm{Fe}((R)\text{-}L^2i\mathrm{Pr})_2]^{2+}$,[15] $[\mathrm{Fe}((R)\text{-}L^1t\mathrm{Bu})_2]^{2+}$ and $[\mathrm{Fe}((R)\text{-}L^2t\mathrm{Bu})_2]^{2+}$ lie within 1.5° of their crystallographic values. The slightly greater θ distortion in crystal structures of low-spin $[\mathrm{Fe}((R)\text{-}L^1\mathrm{Ph})_2]^{2+}$, compared to $[\mathrm{Fe}((R)\text{-}L^2\mathrm{Ph})_2]^{2+}$, is also mirrored in the calculations.

The molecules bearing *iso*propyl groups were hard to minimize since, crystallographically, those substituents have significant rotational freedom.[15,24] Two higher energy local minima were identified for homochiral $[\mathrm{Fe}((R)\text{-}L^1i\mathrm{Pr})_2]^{2+}$ and $[\mathrm{Fe}((R)\text{-}L^2i\mathrm{Pr})_2]^{2+}$ (Table S12, Figures S52-S53). These structures are only 1-2 kcal mol^{-1} above the true minimum for the L^2iPr complex in its preferred high-spin state, implying they should be energetically accessible at room temperature. Thus, the crystal structure of $[\mathrm{Fe}((R)\text{-}L^2i\mathrm{Pr})_2][\mathrm{ClO_4}]_2$ resembles one of these higher energy conformations, rather than its computed minimum structure (Figure S52).[15] For $[\mathrm{Fe}((R)\text{-}L^1i\mathrm{Pr})_2]^{2+}$, the other conformations lie higher above the minimum structure, and less likely to be observed in practise (Table S13).

The minimized heterochiral complexes have more regular coordination geometries, which are also a good match for experiment in most cases. The sole exception is high-spin $[\mathrm{Fe}((R)\text{-}L^2i\mathrm{Pr})((S)\text{-}L^2i\mathrm{Pr})]^{2+}$, which minimized to a conformation resembling that in Figure 2. However, its published crystal structure has a more distorted molecular geometry with a less regular distribution of *i*Pr group orientations.[15] This high-spin molecule may show a similar conformational flexibility to its homochiral isomer.

Other structural features reproduced by the calculations include puckering of the L^1H thiazoline rings, in contrast with the essentially planar oxazoline rings in L^2H (Figures S44 and S48). That difference is found crystallographically in $[\mathrm{Fe}(L^1\mathrm{H})_2]^{2+}$ and $[\mathrm{Fe}(L^2\mathrm{H})_2]^{2+}$ salts,[15,31] and is also evident when the other minimized molecules are compared. The greater conformational flexibility of the L^1R thiazoline groups influences the orientations of their 'R' substituents when R ≠ H, which is easiest to quantify when R = Ph. However, this flexibility is overestimated in the heterochiral $[\mathrm{Fe}(L^1\mathrm{Ph})_2]^{2+}$ and $[\mathrm{Fe}(L^2\mathrm{Ph})_2]^{2+}$ minimizations, which both predict a larger canting of the phenyl substituents than is found experimentally (Table 1). The minimized phenyl group orientations in the homochiral isomers of those complexes are closer to the crystallographic structures.

To compensate for overstabilization of the low-spin form by the GGA functional B86PW91,[51,52] the spin state energies in Table 2 are expressed as $\Delta E_{\mathrm{rel}}\{\mathrm{HS\text{-}LS}\}$, relative to $[\mathrm{Fe}(L^2\mathrm{H})_2]^{2+}$ which shows $T_{1/2}$ = 245 ±2 K in solution.[15] A complex with a positive $\Delta E_{\mathrm{rel}}\{\mathrm{HS\text{-}LS}\}$ has a more stable low-spin state than for $[\mathrm{Fe}(L^2\mathrm{H})_2]^{2+}$, and *vice versa*. The correlation between $\Delta E_{\mathrm{rel}}\{\mathrm{HS\text{-}LS}\}$ and measured $T_{1/2}$ values shows the calculations reproduce the experimental spin state properties reasonably well (Figure 7).[9,12,47] However, the calculations predict the high-spin state of both isomers of $[\mathrm{Fe}(L^1i\mathrm{Pr})_2]^{2+}$ is *ca.*1.5 kcal mol^{-1} more stable than observed experimentally, when compared to the other molecules in the study. This is discussed further below. The computed spin state energies of $[\mathrm{Fe}(L^2i\mathrm{Pr})_2]^{2+}$ and the

Table 1 The average dihedral angle (deg) between the least squares planes of each Ph group and the pyridyl ring on the other ligand, in the experimental and calculated low-spin forms of $[\mathrm{Fe}L_2]^{2+}$ (L = L^1Ph and L^2Ph). The dihedral angles would be zero if these groups perfectly sandwiched each other (Figure 6).

	L = L^1Ph	L = L^2Ph
Homochiral		
Crystallographic[a]	5.1(9)-11.8(2)	12.0(2)-17.9(2)
B86PW91	9.5	10.2
B97-D2	7.2	5.7
Heterochiral		
Crystallographic[a]	13.3(3)-13.5(3)	3.3(2)-6.0(2)
B86PW91	18.4	11.0
B97-D2	9.4	1.5

[a] Range of values for all available crystal structures of these complexes (Tables S4 and S5).

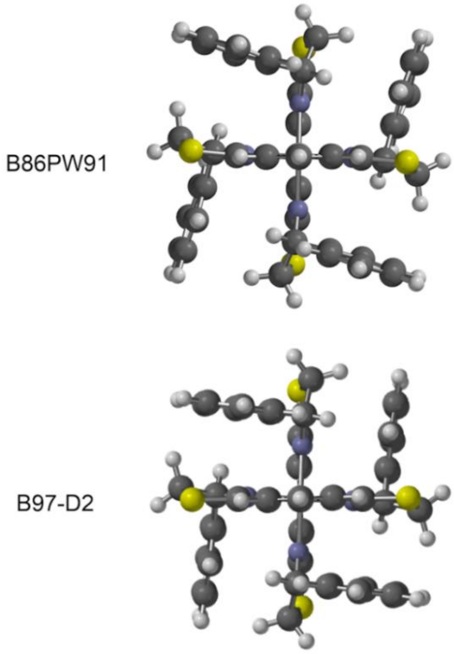

Figure 6 Computed structures of low-spin $[\mathrm{Fe}((R)\text{-}L^1\mathrm{Ph})((S)\text{-}L^1\mathrm{Ph})]^{2+}$, minimized in the gas phase using the B86PW91 (top) and B97-D2 (bottom) functionals. Color code: C, dark gray; H, white; Fe, pale gray; N, blue; S, yellow.

*t*Bu-substituted complexes might contain a similar error, although that would not affect their predicted high-spin nature. In other respects, the data in Table 2 are self-consistent and allow some conclusions to be drawn.

The low-spin state of each $[\mathrm{Fe}(L^1\mathrm{R})_2]^{2+}$ molecule is stabilized compared to its $[\mathrm{Fe}(L^2\mathrm{R})_2]^{2+}$ congener (Table 2). This mostly reflects the d_{z^2} and d_{xy} orbital energies, which are both higher in low-spin $[\mathrm{Fe}(L^1\mathrm{H})_2]^{2+}$ than for $[\mathrm{Fe}(L^2\mathrm{H})_2]^{2+}$ implying stronger Fe–N σ-bonding in the L^1H complex (Figure 8). Consistent with that, the average energy of the lone pair combination orbitals in metal-free L^1H is 0.07 eV higher than for L^2H by the same computational protocol, showing L^1H is the more basic N-donor (Figure S45). In contrast, the average energies of the t_{2g} orbitals in the complexes are almost identical, showing they experience similar levels of metal-ligand π-bonding. Hence, the more low-spin character of $[\mathrm{Fe}(L^1\mathrm{R})_2]^{2+}$ simply reflects the higher Brønsted basicity of that ligand family.

The high-spin state is stabilized in each homochiral complex relative to its heterochiral diastereomer, as expected. However, ΔE_{rel}\{HS-LS\} for homochiral and heterochiral $[\mathrm{Fe}(L^2\mathrm{Ph})_2]^{2+}$ differ by only 0.2 kcal mol^{-1}. This is barely outside the margin of error, but is consistent with another recent study of those molecules.[21] The equivalent energy difference for $[\mathrm{Fe}(L^1\mathrm{Ph})_2]^{2+}$ is ten times larger at 2.0 kcal mol^{-1}, implying a greater discrimination of spin state between those diastereomers as observed experimentally.

Interestingly, the ΔE_{rel}\{HS-LS\} values imply the opposite result for the *iso*propyl complexes, that ΔE_{rel}\{HS-LS\} for homochiral and heterochiral $[\mathrm{Fe}(L^1i\mathrm{Pr})_2]^{2+}$ should be *more* similar than for $[\mathrm{Fe}(L^2i\mathrm{Pr})_2]^{2+}$. That can't be confirmed experimentally however, since both isomers of $[\mathrm{Fe}(L^2i\mathrm{Pr})_2]^{2+}$ are fully high-spin. As described above, it's also less clear how well the spin states of the *i*Pr-substituted complexes are modelled by these calculations (Figure 7).

Table 2 Minimized gas-phase spin state energies for $[\mathrm{Fe}(L^1\mathrm{R})_2]^{2+}$ and $[\mathrm{Fe}(L^2\mathrm{R})_2]^{2+}$ (R = H, Ph, *i*Pr or *t*Bu) using the B86PW91 functional. Experimental solution-phase SCO mid-point temperatures ($T_{½}$) are also given, for comparison (HS = high-spin, LS = low-spin).

		$T_{½}$, K	E(HS), Ha	E(LS), Ha	ΔE_{rel}\{HS-LS\}, kcal mol^{-1} [a]	ΔE\{dia, HS\}, kcal mol^{-1} [b]	ΔE\{dia, LS\}, kcal mol^{-1} [b]
1	$[\mathrm{Fe}(L^1\mathrm{H})_2]^{2+}$	LS[c,d]	−4035.468705	−4035.503406	+5.8	–	–
2	$[\mathrm{Fe}((R)\text{-}L^1\mathrm{Ph})_2]^{2+}$	344(6)	−4959.373908	−4959.400465	+0.7	+0.7	+2.7
3	$[\mathrm{Fe}((R)\text{-}L^1\mathrm{Ph})((S)\text{-}L^1\mathrm{Ph})]^{2+}$	LS[c]	−4959.375037	−4959.404693	+2.7	–	–
4	$[\mathrm{Fe}((R)\text{-}L^1i\mathrm{Pr})_2]^{2+}$	277(1)	−4507.045026	−4507.068592	−1.1	+1.0	+2.3
5	$[\mathrm{Fe}((R)\text{-}L^1i\mathrm{Pr})((S)\text{-}L^1i\mathrm{Pr})]^{2+}$	LS[c]	−4507.046550	−4507.072196	+0.2	–	–
6	$[\mathrm{Fe}((R)\text{-}L^1t\mathrm{Bu})_2]^{2+}$	HS[e]	−4664.211827	−4664.216828	−12.8	−11.1	−12.8
7	$[\mathrm{Fe}((R)\text{-}L^1t\mathrm{Bu})((S)\text{-}L^1t\mathrm{Bu})]^{2+}$	–	−4664.194130	−4664.196372	−14.5	–	–
8	$[\mathrm{Fe}(L^2\mathrm{H})_2]^{2+}$	245(2)[f]	−2743.727948	−2743.753346	0	–	–
9	$[\mathrm{Fe}((R)\text{-}L^2\mathrm{Ph})_2]^{2+}$	244(2)[f]	−3667.635387	−3667.660670	−0.1	+4.7	+4.9
10	$[\mathrm{Fe}((R)\text{-}L^2\mathrm{Ph})((S)\text{-}L^2\mathrm{Ph})]^{2+}$	278(2)[f]	−3667.642858	−3667.668452	+0.1	–	–
11	$[\mathrm{Fe}((R)\text{-}L^2i\mathrm{Pr})_2]^{2+}$	HS[e,f]	−3215.310328	−3215.320134	−9.8	+2.4	+8.6
12	$[\mathrm{Fe}((R)\text{-}L^2i\mathrm{Pr})((S)\text{-}L^2i\mathrm{Pr})]^{2+}$	HS[e,f]	−3215.314169	−3215.333782	−3.6	–	–
13	$[\mathrm{Fe}((R)\text{-}L^2t\mathrm{Bu})_2]^{2+}$	HS[e]	−3372.489865	−3372.491425	−15.0	−5.6	−6.8
14	$[\mathrm{Fe}((R)\text{-}L^2t\mathrm{Bu})((S)\text{-}L^2t\mathrm{Bu})]^{2+}$	–	−3372.480884	−3372.480526	−16.2	–	–

[a] A positive ΔE_{rel}\{HS–LS\} means the low-spin state is more stable than for $[\mathrm{Fe}(L^2\mathrm{H})_2]^{2+}$, and *vice versa*. [b] A positive ΔE\{dia\} means the heterochiral isomer is more stable than the homochiral form by this protocol, and *vice versa*. [c] The complex is diamagnetic and fully low-spin by NMR at room temperature, implying $T_{½} \geq 400$ K (ref. 46). [d] Ref. 31. [e] The complex is fully high-spin over the temperature range of the measurement. [f] Ref. 15.

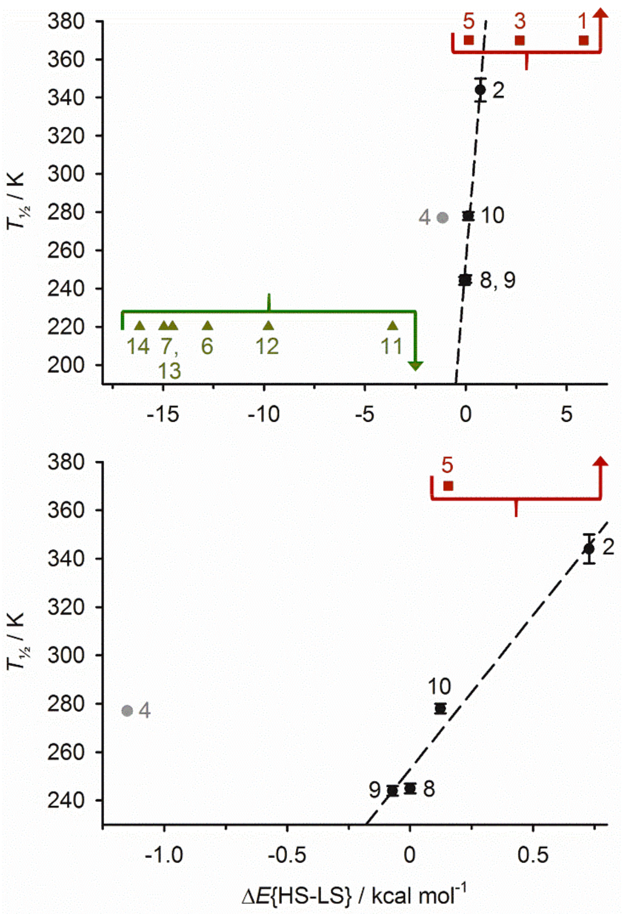

Figure 7 Top: correlation between measured solution $T_{½}$ values, and the computed spin state energies in Table 2. Each data point is identified by the corresponding entry in the Table, and the line shows the best fit linear regression of the black data points. Compounds showing SCO near room temperature are black or gray circles; low-spin compounds ($T_{½} > 350$ K) are red squares, and high-spin compounds ($T_{½} < 220$ K) are green triangles. Bottom: expansion of the top graph, highlighting the SCO-active molecules.

The heterochiral isomer of each phenyl and *iso*-propyl substituted molecule has lower energy than its homochiral analogue, according to the energy difference between them ΔE\{dia\} (Table 2). The difference is larger in the low-spin complexes, whose shorter Fe–N bonds and more regular co-ordination geometries place their 'R' substituents closer together. In contrast, ΔE\{dia\} shows the homochiral isomer is more stable for $[Fe(L^1tBu)_2]^{2+}$ and $[Fe(L^2tBu)_2]^{2+}$, which explains our inability to prepare the heterochiral form of $[Fe(L^1tBu)_2][ClO_4]_2$.

The overstabilized high-spin state of $[Fe((R)\text{-}L^1iPr)_2]^{2+}$ and $[Fe((R)\text{-}L^1iPr)((S)\text{-}L^1iPr)]^{2+}$ (Figure 7) might reflect that B86PW91 doesn't include dispersion interactions between non-bonded atoms, which could be significant in crowded molecules like these.[53] To test that, the calculations were repeated with another GGA functional that includes a dispersion correction, B97-D2.[54] While absolute energies calculated by these two functionals will differ, computational surveys imply they should yield consistent ΔE_{rel}\{HS-LS\} values, other things being equal.[49,51,55]

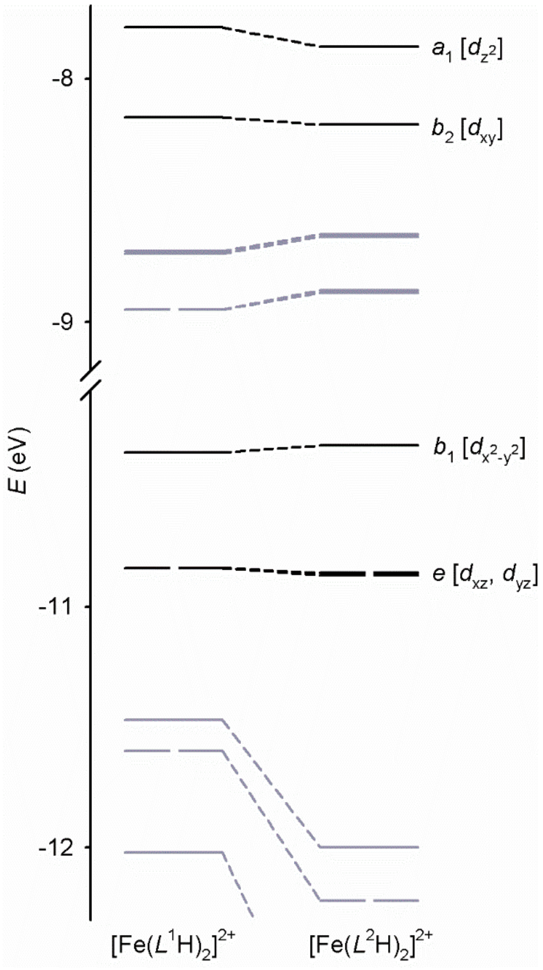

Figure 8 Frontier MO energies of low-spin $[Fe(L^1H)_2]^{2+}$ and $[Fe(L^2H)_2]^{2+}$ computed with the B86PW91 functional. The energy levels are color coded as: metal-based *d*-orbitals (black); and ligand-centered MOs (gray). Plots of these MOs are in Figures S57 and S58, and the *d*-orbitals are labelled in the idealized D_{2d} symmetry for this ligand geometry.

The minimized ΔE_{rel}\{HS-LS\} for $[Fe(L^1H)_2]^{2+}$ computed by B97-D2 is +6.3 kcal mol^{-1}, which resembles the +5.8 kcal mol^{-1} value from B86PW91 (Table S14). However, the dispersion-corrected functional over-stabilizes the low-spin states of $[Fe(L^1R)_2]^{2+}$ and $[Fe(L^2R)_2]^{2+}$ when R = Ph or *i*Pr, by up to 7 kcal mol^{-1}. Moreover, the B97-D2 calculations reveal two other inconsistencies. First, they compute the low-spin state of $[Fe((R)\text{-}L^2Ph)_2]^{2+}$ to be more stable than for its heterochiral counterpart. Second, ΔE\{dia\} for heterochiral $[Fe((R)\text{-}L^1Ph)((S)\text{-}L^1Ph)]^{2+}$ is computed to be negative, which would make it unstable to racemization through ligand exchange. Neither of these anomalies occurs in the B86PW91 energies, which are a better match for the experimental results.[54]

Notably, the B97-D2 minimizations of the phenyl-substituted complexes include tighter intramolecular $\pi\cdots\pi$ stacking of their phenyl and pyridyl groups than in the B86PW91 minimizations (Figures 6, S60 and S61). This is most marked in the heterochiral isomers, where $\pi\cdots\pi$ stacking of the phenyl groups is under-estimated by the B86PW91 minimizations, but overestimated by B97-D2, when compared with experiment (Table 1, Figure 6). For homochiral $[\mathrm{Fe}((R)\text{-}L^{2}\mathrm{Ph})_{2}]^{2+}$ this $\pi\cdots\pi$ stacking is also much stronger by B97-D2 than is observed experimentally; the $\pi\cdots\pi$ interactions are apparently strong enough to overcome steric clashes between Ph groups with this functional. That may contribute to the overstabilized low-spin state in the B97-D2 minimization of this molecule.

We conclude dispersion interactions should make a. small contribution to the spin-state energies of $[\mathrm{Fe}(L^{1}\mathrm{R})_{2}]^{2+}$ and $[\mathrm{Fe}(L^{2}\mathrm{R})_{2}]^{2+}$ but, if so, this is over-estimated by the B97-D2 functional in these gas-phase calculations.[54]

Conclusion

The low-spin state of $[\mathrm{Fe}(L^{1}\mathrm{R})_{2}]^{2+}$ (R = H, Ph or *i*Pr) is consistently stabilized compared to the corresponding $[\mathrm{Fe}(L^{2}\mathrm{R})_{2}]^{2+}$ compounds, for a given 'R' substituent (Table 2). That mostly reflects the greater σ-basicity of the thiazoline N-donor atoms in $L^{1}\mathrm{R}$, compared to the oxazoline rings in $L^{2}\mathrm{R}$ (Figure 8). Moreover, the previously reported steric stabilization of the high-spin state in $[\mathrm{Fe}((R)\text{-}L^{2}\mathrm{Ph})_{2}]^{2+}$, compared to its heterochiral diastereomer,[15] is enhanced in $[\mathrm{Fe}(L^{1}\mathrm{Ph})_{2}]^{2+}$. That could not be quantified experimentally however, since SCO in the heterochiral complex lies outside the liquid range of common NMR solvents.

The 'R' substituents exert greater steric influence on the spin states and stabilities of $[\mathrm{Fe}(L^{1}\mathrm{R})_{2}]^{2+}$ than on $[\mathrm{Fe}(L^{2}\mathrm{R})_{2}]^{2+}$. That is evident in the spin state properties of the diastereomers of $[\mathrm{Fe}(L^{1}\mathrm{Ph})_{2}]^{2+}$, as above, and also in their coordination geometries which are consistently more distorted in crystals of homochiral $[\mathrm{Fe}(L^{1}\mathrm{Ph})_{2}]^{2+}$ than for $[\mathrm{Fe}(L^{2}\mathrm{Ph})_{2}]^{2+}$. It also reflects that $[\mathrm{Fe}((S)\text{-}L^{1}i\mathrm{Pr})_{2}]^{2+}$ and $[\mathrm{Fe}((S)\text{-}L^{1}t\mathrm{Bu})_{2}]^{2+}$ undergo significant ligand displacement in $\mathrm{CD_3CN}$ solution, while $[\mathrm{Fe}((S)\text{-}L^{2}i\mathrm{Pr})_{2}]^{2+}$ [15] and $[\mathrm{Fe}((S)\text{-}L^{2}t\mathrm{Bu})_{2}]^{2+}$ do not.

Homochiral $[\mathrm{Fe}((S)\text{-}L^{1}t\mathrm{Bu})_{2}]^{2+}$ and $[\mathrm{Fe}((S)\text{-}L^{2}t\mathrm{Bu})_{2}]^{2+}$ are unexpectedly stable as their perchlorate salts, despite their steric crowding. Both cations are high-spin with highly distorted coordination geometries, which reflects the steric influence of their *t*Bu groups (Figure 3). The heterochiral diastereomers of those complexes could not be isolated or observed in solution, however. This was reproduced computationally, which showed heterochiral $[\mathrm{Fe}((R)\text{-}L^{1}\mathrm{R})((S)\text{-}L^{1}\mathrm{R})]^{2+}$ and $[\mathrm{Fe}((R)\text{-}L^{2}\mathrm{R})((S)\text{-}L^{2}\mathrm{R})]^{2+}$ are more stable in the gas phase than their homochiral congeners for R = Ph and *i*Pr, but are less stable for R = *t*Bu.

The gas phase DFT calculations also confirm other aspects of this work. Although their ligand conformations aren't all perfectly reproduced (Table 1), the spin state energies and coordination geometries of $[\mathrm{Fe}(L^{1}\mathrm{R})_{2}]^{2+}$ and $[\mathrm{Fe}(L^{2}\mathrm{R})_{2}]^{2+}$ are self-consistent and agree with experiment, when R = H, Ph and *t*Bu (Figure 7; Tables S10 and S11). However, the calculations are less successful for R = *i*Pr, since the high-spin state of both diastereomers of $[\mathrm{Fe}(L^{1}i\mathrm{Pr})_{2}]^{2+}$ is over-stabilized by *ca* 1.5 kcal mol^{-1} compared to the complexes with R = H and Ph. Moreover, the difference between $\Delta E_{\mathrm{rel}}\{\mathrm{HS\text{-}LS}\}$ of the two diastereomers is computed to be larger for $[\mathrm{Fe}(L^{1}\mathrm{R})_{2}]^{2+}$ than $[\mathrm{Fe}(L^{2}\mathrm{R})_{2}]^{2+}$ when R = Ph, but smaller when R = *i*Pr. The computed trend for R = Ph agrees with experiment, but cannot be confirmed for R = *i*Pr because both diastereomers of $[\mathrm{Fe}(L^{2}i\mathrm{Pr})_{2}]^{2+}$ are high-spin. Hence, it is unclear how well $[\mathrm{Fe}(L^{1}i\mathrm{Pr})_{2}]^{2+}$ and $[\mathrm{Fe}(L^{2}i\mathrm{Pr})_{2}]^{2+}$ are treated by our calculations.

The anomalous spin state energies for R = *i*Pr could reflect the influence of intramolecular dispersion interactions involving the 'R' substituents, which are not treated by the B86PW91 functional. Dispersion interaction energies should favor the more compact low-spin state, which brings non-bonded atoms in a molecule closer together.[55] However, repeat calculations using the dispersion-corrected functional B97-D2 over-correct for this, in computing a much greater low-spin character for $[\mathrm{Fe}(L^{1}\mathrm{R})_{2}]^{2+}$ and $[\mathrm{Fe}(L^{2}\mathrm{R})_{2}]^{2+}$ (R = Ph and *i*Pr) than is observed experimentally.[54] They also predict the wrong relationship between the diastereomers for $[\mathrm{Fe}(L^{2}\mathrm{Ph})_{2}]^{2+}$ (Table S14). The intramolecular $\pi\cdots\pi$ interactions computed by this functional when R = Ph are stronger in the B97-D2 minimizations than observed experimentally, which may contribute to that anomaly (Table 1).

Common methods of treating dispersion in DFT are known to overstabilize the low-spin states of SCO molecules. That may reflect the absence of intermolecular dispersion interactions in single molecule calculations, which leads to overestimation of the intramolecular dispersion contribution.[55] Our calculations suggest these errors are exacerbated in sterically crowded molecules, involving intramolecular contacts between peripheral substituents.

These results give additional insights into the interplay between chirality and spin state in sterically crowded iron(II) complexes. As well as having value for the synthesis of chiral SCO materials,[16] they have wider relevance for the design of chiral iron catalysts or chromophores, which are tailored to adopt the correct spin state properties for the desired application.[1-3]

ASSOCIATED CONTENT

Supporting Information.

The Supporting Information is available free of charge on the ACS Publications website at DOI: 10.1021/acs.inorgchem.#####.

> Synthetic procedures and characterization data for the $L^{1}\mathrm{R}$ ligands; crystallographic data and refinement procedures; crystallographic Figures and Tables; X-ray powder diffraction patterns and additional solid state magnetic data; paramagnetic NMR spectra (PDF).
>
> Details of the minimized structures from the DFT calculations, atomic coordinates and frontier orbital plots (PDF).

Accession Codes

CCDC 2091639-2091642, 2091644-2091649 and 2091658-2091661 contain the supplementary crystallographic data for this paper. These data can be obtained free of charge via www.ccdc.cam.ac.uk/data_request/cif, or by emailing data_request@ccdc.cam.ac.uk, or by contacting The Cambridge Crystallographic Data Centre, 12 Union Road, Cambridge CB2 1EZ, UK; fax: +44 1223 336033.

Data Sets

Experimental data sets associated with this paper are available from the University of Leeds library (http://doi.org/10.5518/###).

AUTHOR INFORMATION

Corresponding Author

*E-mail for M.A.H.: m.a.halcrow@leeds.ac.uk.

Present Address

|| Department of Chemistry, University of Durham, Durham DH1 3LE, UK.
¶ Department of Chemical Sciences, University of Huddersfield, Huddersfield HD1 3DH, UK.

Author Contributions

All authors have given approval to the final version of the manuscript.

Notes

The authors declare no competing financial interest.

ACKNOWLEDGMENT

This work was funded by the EPSRC (EP/N509681/1) and the Leverhulme Trust (RPG-2015-095). We also thank Diamond Light Source for access to beamline I19 (MT20570), which contributed to the results presented here.

REFERENCES

(1) (a) Wenger, O. S. Is Iron the New Ruthenium? *Chem. Eur. J.* **2019**, *25*, 6043–6052. (b) Förster, C.; Heinze, K. Photophysics and Photochemistry with Earth- Abundant Metals – Fundamentals and Concepts. *Chem. Soc. Rev.* **2020**, *49*, 1057–1070.

(2) (a) Chirik, P.; Morris, R. Getting Down to Earth: The Renaissance of Catalysis with Abundant Metals. *Acc. Chem. Res.* **2015**, *48*, 2495. (b) Beller, M. Introduction: First Row Metals and Catalysis. *Chem. Rev.* **2019**, *119*, 2089.

(3) Halcrow, M. A. Manipulating Metal Spin States for Biomimetic, Catalytic and Molecular Materials Chemistry. *Dalton Trans.* **2020**, *49*, 15560–15567.

(4) (a) Filonenko, G. A.; van Putten, R.; Hensen, E. J. M.; Pidko, E. A. Catalytic (De)Hydrogenation Promoted by Non-Precious Metals – Co, Fe and Mn: Recent Advances in an Emerging Field. *Chem. Soc. Rev.* **2018**, *47*, 1459–1483. (b) Wei , D.; Darcel, C. Iron Catalysis in Reduction and Hydrometalation Reactions. *Chem. Rev.* **2019**, *119*, 2550–2610.

(5) (a) Bedford, R. B. How Low Does Iron Go? Chasing the Active Species in Fe-Catalyzed Cross-Coupling Reactions. *Acc. Chem. Res.* **2015**, *48*, 1485–1493. (b) Neidig, M. L.; Carpenter, S. H.; Curran, D. J.; DeMuth, J. C.; Fleischauer, V. E.; Iannuzzi, T. E.; Neate, P. G. N.; Sears, J. D.; Wolford, N. J. Development and Evolution of Mechanistic Understanding in Iron-Catalyzed Cross-Coupling. *Acc. Chem. Res.* **2019**, *52*, 140–150.

(6) Guo, M.; Corona, T.; Ray, K.; Nam, W. Heme and Nonheme High-Valent Iron and Manganese Oxo Cores in Biological and Abiological Oxidation Reactions. *ACS Cent. Sci.* **2019**, *5*, 13–28.

(7) (a) Harvey, J. N.; Poli, R.; Smith, K. M. Understanding the Reactivity of Transition Metal Complexes Involving Multiple Spin States. *Coord. Chem. Rev.* **2003**, *238-239*, 347–361. (b) Holland, P. L. Distinctive Reaction Pathways at Base Metals in High-Spin Organometallic Catalysts. *Acc. Chem. Res.* **2015**, *48*, 1696–1702.

(8) Kershaw Cook, L. J.; Mohammed, R.; Sherborne, G.; Roberts, T. D.; Alvarez, S.; Halcrow, M. A. Spin State Behaviour of Iron(II)/Dipyrazolylpyridine Complexes. New Insights from Crystallographic and Solution Measurements. *Coord. Chem. Rev.* **2015**, *289-290*, 2–12.

(9) Kershaw Cook, L. J.; Kulmaczewski, R.; Mohammed, R.; Dudley, S.; Barrett, S. A.; Little, M. A.; Deeth, R. J.; Halcrow, M. A. A Unified Treatment of the Relationship Between Ligand Substituents and Spin State in a Family of Iron(II) Complexes. *Angew. Chem., Int. Ed.* **2016**, *55*, 4327–4331.

(10) Kimura, A.; Ishida, T. Pybox-Iron(II) Spin-Crossover Complexes with Substituent Effects from the 4-Position of the Pyridine Ring (Pybox = 2,6-Bis(oxazolin-2-yl)pyridine). *Inorganics* **2017**, *5*, 52.

(11) See also: (a) Tweedle, M. F.; Wilson, L. J. Variable Spin Iron(III) Chelates with Hexadentate Ligands Derived from Triethylenetetramine and Various Salicylaldehydes. Synthesis, Characterization, and Solution State Studies of a New $^2T \leftrightarrow {}^6A$ Spin Equilibrium System. *J. Am. Chem. Soc.* **1976**, *98*, 4824–4834. (b) Petty, R. H.; Dose, E. V.; Tweedle, M. F.; Wilson, L. J. Bis(*N*-methylethylenediaminesalicylaldiminato)iron(III) Complexes. Magnetic, Mossbauer, and Intersystem Crossing Rate Studies in the Solid and Solution States for a New ($S = 1/2$) ↔ ($S = 5/2$) Spin-Equilibrium Case. *Inorg. Chem.* **1978**, *17*, 1064–1071. (c) Nakano, K.; Suemura, N.; Yoneda, K.; Kawata, S.; Kaizaki, S. Substituent Effect of the Coordinated Pyridine in a Series of Pyrazolato Bridged Dinuclear Diiron(II) Complexes on the Spin-Crossover Behavior. *Dalton Trans.* **2005**, *2005*, 740–743. (d) Prat, I.; Company, A.; Corona, T.; Parella, T.; Ribas, X.; Costas, M. Assessing the Impact of Electronic and Steric Tuning of the Ligand in the Spin State and Catalytic Oxidation Ability of the Fe^{II}(Pytacn) Family of Complexes. *Inorg. Chem.* **2013**, *52*, 9229–9244. (e) Kumar, K. S.; Vela, S.; Heinrich, B.; Suryadevara, N.; Karmazin, L.; Bailly, C.; Ruben, M. Bi-Stable Spin-Crossover in Charge-Neutral $[Fe(R\text{-}ptp)_2]$ (ptp = 2-(1*H*-pyrazol-1-yl)-6-(1*H*-tetrazol-5-yl)pyridine) Complexes. *Dalton Trans.* **2020**, *49*, 1022–1031. (f) Milocco, F.; de Vries, F.; Bartels, I. M. A.; Havenith, R. W. A.; Cirera, J.; Demeshko, S.; Meyer, F.; Otten, E. Electronic Control of Spin-Crossover Properties in Four-Coordinate Bis(formazanate) Iron(II) Complexes. *J. Am. Chem. Soc.* **2020**, *142*, 20170–20181.

(12) Capel Berdiell, I.; Kulmaczewski, R.; Halcrow, M. A. Iron(II) Complexes of 2,4-Dipyrazolyl-1,3,5-triazine Derivatives – the Influence of Ligand Geometry on Metal Ion Spin state. *Inorg. Chem.* **2017**, *56*, 8817–8828.

(13) See also: (a) Phan, H.; Hrudka, J. J.; Igimbayeva, D.; Daku, L. M. L.; Shatruk, M. A Simple Approach for Predicting the Spin State of Homoleptic Fe(II) Tris-diimine Complexes. *J. Am. Chem. Soc.* **2017**, *139*, 6437–6447. (b) McPherson, J. N.; Elton, T. E.; Colbran, S. B. A Strain-Deformation Nexus within Pincer Ligands: Application to the Spin States of Iron(II) Complexes. *Inorg. Chem.* **2018**, *57*, 12312–12322.

(14) Halcrow, M. A.; Capel Berdiell, I.; Pask, C. M.; Kulmaczewski, R. Relationship between the Molecular Structure and Switching Temperature in a Library of Spin-Crossover Molecular Materials. *Inorg. Chem.* **2019**, *58*, 9811–9821.

(15) Burrows, K. E.; McGrath, S. E.; Kulmaczewski, R.; Cespedes, O.; Barrett, S. A.; Halcrow, M. A. Spin States of Homochiral and Heterochiral Isomers of $[Fe(PyBox)_2]^{2+}$ Derivatives. *Chem. Eur. J.* **2017**, *23*, 9067–9075.

(16) Chiral SCO materials have also been investigated in the solid state. These have potential to show switchable ferroelectric[56] or chiroptical properties,[57] but are less informative about the influence of chirality on spin state at the molecular level. See *eg* (a) Gural'skiy, I. A.; Reshetnikov, V. A.; Szebesczyk, A.; Gumienna-Kontecka, E.; Marynin, A. I.; Shylin, S. I.; Ksenofontov, V.; Fritsky, I. O. Chiral Spin Crossover Nanoparticles and Gels with Switchable Circular Dichroism. *J. Mater. Chem. C* **2015**, *3*, 4737–4741. (b) Gural'skiy, I. A.; Kucheriv, O. I.; Shylin, S. I.; Ksenofontov, V.; Polunin, R. A.; Fritsky, I. O. Enantioselective Guest Effect on the Spin State of a Chiral Coordination Framework. *Chem. Eur. J.* **2015**, *21*, 18076–18079. (c) Wang, Q.; Venneri, S.; Zarrabi, N.; Wang, H.; Desplanches, C.; Létard, J.-F.; Seda, T.; Pilkington, M. Stereochemistry for Engineering Spin Crossover: Structures and Magnetic Prop-

erties of a Homochiral *vs.* Racemic $[Fe(N_3O_2)(CN)_2]$ Complex. *Dalton Trans.* **2015**, *44*, 6711–6714. (d) Qin, L.-F.; Pang, C.-Y.; Han, W.-K.; Zhang, F.-L.; Tian, L.; Gu, Z.-G.; Ren, X.; Li, Z. Spin Crossover Properties of Enantiomers, Co-Enantiomers, Racemates, and Co-Racemates. *Dalton Trans.* **2016**, *45*, 7340–7348. (e) Sekimoto, Y.; Karim, M. R.; Saigo, N.; Ohtani, R.; Nakamura, M.; Hayami, S. Crystal Structures and Spin-Crossover Behavior of Iron(II) Complexes with Chiral and Racemic Ligands. *Eur. J. Inorg. Chem.* **2017**, *2017*, 1049–1053. (f) Ru, J.; Yu, F.; Shi, P.-P.; Jiao, C.-Q.; Li, C.-H.; Xiong, R.-G.; Liu, T.; Kurmoo, M.; Zuo, J.-L. Three Properties in One Coordination Complex: Chirality, Spin Crossover, and Dielectric Switching. *Eur. J. Inorg. Chem.* **2017**, *2017*, 3144–3149. (g) Bartual-Murgui, C.; Piñeiro-López, L.; Valverde-Muñoz, F. J.; Muñoz, M. C.; Seredyuk, M.; Real, J. A. Chiral and Racemic Spin Crossover Polymorphs in a Family of Mononuclear Iron(II) Compounds. *Inorg. Chem.* **2017**, *56*, 13535–13546. (h) Jakobsen, V. B.; O'Brien, L.; Novitchi, G.; Müller-Bunz, H.; Barra, A,-L.; Morgan, G. G. Chiral Resolution of a Mn^{3+} Spin Crossover Complex. *Eur. J. Inorg. Chem.* **2019**, *2019*, 4405–4411. (i) Ma, T.-T.; Sun, X.-P.; Yao, Z.-S.; Tao, J. Homochiral *versus* Racemic Polymorphs of Spin-Crossover Iron(II) Complexes with Reversible LIESST Effect. *Inorg. Chem. Front.* **2020**, *7*, 1196–1204.

(17) Johnson, J. S.; Evans, D. A. Chiral Bis(oxazoline) Copper(II) Complexes: Versatile Catalysts for Enantioselective Cycloaddition, Aldol, Michael, and Carbonyl Ene Reactions. *Acc. Chem. Res.* **2000**, *33*, 325–335. (b) Desimoni, G.; Faita, G.; Quadrelli, P. Pyridine-2,6-bis(oxazolines), Helpful Ligands for Asymmetric Catalysts. *Chem. Rev.* **2003**, *103*, 3119–3154. (c) Rohit, K. R.; Ujwaldev, S. M.; Saranya, S.; Anilkumar, G. Recent Advances in the Creation of Asymmetric Carbon Centre(s) by Generation of Carbon-Heteroatom Bond(s) Using Metal-Pybox Complexes. *Asian J. Org. Chem.* **2018**, *7*, 2338–2356. (d) Connon, R.; Roche, B.; Rokade, B. V.; Guiry, P. J. Further Developments and Applications of Oxazoline-Containing Ligands in Asymmetric Catalysis. *Chem. Rev.* **2021**, *121*, 6373–6521.

(18) In ref. 15, we referred to homochiral and heterochiral $[Fe(L^2R)_2]^{2+}$ as their *rac* and *meso* isomers, respectively. In this paper we've retained the homochiral and heterochiral nomenclature, to avoid confusion over the racemic homochiral (*rac*) and *meso* heterochiral solvate crystals of "$[Fe((R)\text{-}L^1Ph)((S)\text{-}L^1Ph)]^{2+}$" reported in this work.

(19) For other homoleptic iron complexes of PyBox derivatives see refs. 10, 20, 21 and: (a) Zhu, Y.-Y.; Liu, C. W.; Yin, J.; Meng, Z. S.; Yang, Q.; Wang, J.; Liu, T.; Gao, S. Structural Phase Transition in a Multi-Induced Mononuclear Fe^{II} Spin-Crossover Complex. *Dalton Trans.* **2015**, *44*, 20906–20912. (b) Zhu, Y.-Y.; Li, H.-Q.; Ding, Z.-Y.; Lü, X.-J.; Zhao, L.; Meng, Y.-S.; Liu, T.; Gao, S. Spin Transitions in a Series of $[Fe(Pybox)_2]^{2+}$ Complexes Modulated by Ligand Structures, Counter Anions, and Solvents. *Inorg. Chem. Front.* **2016**, *3*, 1624–1636. (c) Wang, Y.-Q.; Pan, Y.; Gao, W.-Q.; Wu, Y.; Liu, C.-H.; Zhu, Y.-Y. Construction of Optical Active Metallo-Supramolecular Polymers from Enantiopure *Bis*-Pybox Ligands. *Tetrahedron* **2019**, *75*, 3809–3814.

(20) Gao, W.-Q.; Meng, Y.-S.; Liu, C.-H.; Pan, Y.; Liu, T.; Zhu, Y.-Y. Spin Crossover and Structural Phase Transition in Homochiral and Heterochiral $Fe[(pybox)_2]^{2+}$ Complexes. *Dalton Trans.* **2019**, *48*, 6323–6327.

(21) Wang, R.-G.; Meng, Y,-S,; Gao, F.-F.; Gao, W.-Q.; Liu, C.-H.; Li, A.; Liu, T.; Zhu, Y.-Y. Ligand Symmetry Significantly Affect Spin Crossover Behaviour in Isomeric $[Fe(Pybox)_2]^{2+}$ Complexes. *Dalton Trans.* **2021**, *50*, 3369–3378. This paper includes a DFT study of homo- and heterochiral $[Fe(L^2Ph)_2]^{2+}$.

(22) (a) Evans, D. A.; Kozlowski, M. C.; Murry, J. A.; Burgey, C. S.; Campos, K. R.; Connell, B. T.; Staples, R. J. C_2-Symmetric Copper(II) Complexes as Chiral Lewis Acids. Scope and Mechanism of Catalytic Enantioselective Aldol Additions of Enolsilanes to (Benzyloxy)acetaldehyde. *J. Am. Chem. Soc.*, 1999, **121**, 669–685. (b) Saaby, S.; Nakama, K.; Lie, M. A.; Hazell, R. G.; Jørgensen, K. A. The First Catalytic Highly Enantioselective Alkylation of Ketimines – A Novel Approach to Optically Active Quaternary α-Amino Acids. *Chem. Eur. J.* **2003**, *9*, 6145–6154. (c) Sato, H.; Suzuki, Y.; Takai, Y.; Kawasaki, H.; Arakawa, R.; Shizuma, M. Detection of the Heterochirality of a 1:2 Metal/Ph-pybox Complex Ion by ESIMS. *Chem. Lett.* **2010**, *39*, 564–566.

(23) Provent, C.; Bernardinelli, G.; Williams, A. F.; Vulliermet, N. Diastereoselectivity of Octahedral Cobalt(II) Pybox Complexes. *Eur. J. Inorg. Chem.* **2001**, *2001*, 1963–1967

(24) Burrows, K. E.; Kulmaczewski, R.; Cespedes, O.; Barrett, S. A.; Halcrow, M. A. The Speciation of Homochiral and Heterochiral Diastereomers of Homoleptic Cobalt(II) and Zinc(II) Pybox Complexes. *Polyhedron* **2018**, *149*, 134–141.

(25) Abrunhosa, I.; Gulea, M.; Levillain, J.; Masson, S. Synthesis of New Chiral Thiazoline-Containing Ligands. *Tetrahedron: Asymm.* **2001**, *12*, 2851–2859.

(26) (a) Le Maux, P.; Abrunhosa, I.; Berchel, M.; Simonneaux, G.; Gulea, M.; Masson, S. Application of Chiral 2,6-Bis(Thiazolinyl)pyridines in Asymmetric Ru-Catalyzed Cyclopropanations with Diazoesters. *Tetrahedron: Asymm.* **2004**, *15*, 2569–2573. (b) Abrunhosa, I.; Delain-Bioton, L.; Gaumont, A.-C.; Gulea, M.; Masson, S. Chiral Thiazoline Ligands: Application in Pd-Catalysed Allylic Substitution. *Tetrahedron*, 2004, **60**, 9263–9272.

(27) Nishio, T.; Kodama, Y.; Tsurumi, Y. Synthesis of Chiral Bis-Thiazolines and Asymmetric Diels–Alder Reactions. *Phosphorus, Sulfur, and Silicon* **2005**, *180*, 1449–1450.

(28) Nobbs, J. D.; Tomov, A. K.; Cariou, R.; Gibson, V. C.; White, A. J. P.; Britovsek, G. J. P. Thio-Pybox and Thio-Phebox Complexes of Chromium, Iron, Cobalt and Nickel and Their Application in Ethylene and Butadiene Polymerisation Catalysis. *Dalton Trans.* **2012**, *41*, 5949–5964.

(29) Loos, P.; Ronco, C.; Riedrich, M.; Arndt, H.-D. Unified Azoline and Azole Syntheses by Optimized Aza-Wittig Chemistry. *Eur. J. Org. Chem.* **2013**, *2013*, 3290–3315.

(30) Guo, J.; Wang, B.; Bi, J.; Zhang, C.; Zhang, H.; Bai, C.; Hu, Y.; Zhang, X. Synthesis, Characterization and 1,3-Butadiene Polymerization Studies of Cobalt Dichloride Complexes Bearing Pyridine Bisoxazoline Ligands. *Polymer* **2015**, *59*, 124–132.

(31) Pan, Y.; Meng, Y.-S.; Liu, Q.; Gao, W.-Q.; Liu, C.-H.; Liu, T.; Zhu, Y.-Y. Construction of SCO-Active Fe(II) Mononuclear Complexes from the Thio-pybox Ligand. *Inorg. Chem.* **2020**, *59*, 7398–7407.

(32) Sheldrick, G. M. Crystal Structure Refinement with SHELXL. *Acta Crystallogr., Sect. C: Struct. Chem.* **2015**, *71*, 3–8.

(33) Barbour, L. J. X-Seed – A Software Tool for Supramolecular Crystallography. *J. Supramol. Chem.* **2001**, *1*, 189–191.

(34) Dolomanov, O. V.; Bourhis, L. J.; Gildea, R. J.; Howard, J. A. K.; Puschmann, H. OLEX2: a Complete Structure Solution, Refinement and Analysis Program. *J. Appl. Crystallogr.* **2009**, *42*, 339–341.

(35) O'Connor, C. J. Magnetochemistry – Advances in Theory and Experimentation. *Prog. Inorg. Chem.* **2007**, *29*, 203–283.

(36) (a) Evans, D. F. The Determination of the Paramagnetic Susceptibility of Substances in Solution by Nuclear Magnetic Resonance. *J. Chem. Soc.* **1959**, *1959*, 2003–2005. (b) Schubert, E. M. Utilizing the Evans Method with a Superconducting NMR Spectrometer in the Undergraduate Laboratory. *J. Chem. Educ.* **1992**, *69*, 62.

(37) García, B.; Ortega, J. C. Excess Viscosity η^E, Excess Volume V^E, and Excess Free Energy of Activation ΔG^{*E} at 283, 293, 303, 313, and 323 K for Mixtures of Acetonitrile and Alkyl Benzoates. *J. Chem. Eng. Data* **1988**, *33*, 200–204.

(38) Equation 1 is a rearrangement of $\Delta G = -RT \ln K$, where K is the ratio of high-spin and low-spin molecules in the sample at temperature T, and $\Delta G = \Delta H - T\Delta S$. Equation 2 reflects that, at $T_{1/2}$, the SCO is at equilibrium so that $\Delta G = 0$ and $\Delta H = T_{1/2}\Delta S$.

(39) *Spartan'18*; Wavefunction Inc.: Irvine, CA, 2018.

(40) The ligand planes defining θ are usually calculated using all the non-H atoms from each tridentate ligand, which works well if the azoline rings are essentially planar. However, since the thiazoline rings in L^1R are puckered, that approach over-estimated the distortion of the inner coordination sphere in $[Fe(L^1R)_2]^{2+}$. Hence, in this study only the least squares planes formed by the coplanar

pyridyl and thiazoline C=N groups of each ligand are used to calculate θ. The Supporting Information includes revised θ values for the $[\mathrm{Fe}(L^2\mathrm{R})_2]^{2+}$ complexes in ref.15, which have been recalculated by this new approach to allow meaningful comparison.

(41) (a) König, E. Structural Changes Accompanying Continuous and Discontinuous Spin-State Transitions. *Prog. Inorg. Chem.* **1987**, *35*, 527–622. (b) Halcrow, M. A. Structure:Function Relationships in Molecular Spin-Crossover Complexes. *Chem. Soc. Rev.* **2011**, *40*, 4119–4142.

(42) (a) Holland, J. M.; McAllister, J. A.; Kilner, C. A.; Thornton-Pett, M.; Bridgeman, A. J.; Halcrow, M. A. Stereochemical Effects on the Spin-State Transition Shown by Salts of $[\mathrm{FeL}_2]^{2+}$[L = 2,6-Di(pyrazol-1-yl)pyridine]. *J. Chem. Soc., Dalton Trans.* **2002**, *2002*, 548–554. (b) Vela, S.; Novoa, J. J.; Ribas-Arino, J. Insights into the Crystal-Packing Effects on the Spin Crossover of $[\mathrm{Fe^{II}(1\text{-}bpp)_2}]^{2+}$-Based Materials. *Phys. Chem. Chem. Phys.* **2014**, *16*, 27012–27024.

(43) The completeness of SCO transitions that are incomplete within the temperature range of the measurement, was estimated assuming $\chi_M T$ = 3.5 cm^3 mol^{-1} K for the fully high-spin state and $\chi_M T = 0$ for the low-spin form. Iron(II) complexes of meridional tridentate ligands typically exhibit $\chi_M T$ within ±0.1 cm^3 mol^{-1} K of those values.[8,58]

(44) See *eg* (a) Clemente-León, M.; Coronado, E.; Giménez-López, M. C.; Romero, F. M. Structural, Thermal, and Magnetic Study of Solvation Processes in Spin-Crossover $[\mathrm{Fe(bpp)_2}][\mathrm{Cr(L)(ox)_2}]_2\cdot\mathrm{H_2O}$ Complexes. *Inorg. Chem.* **2007**, *46*, 11266–11276. (b) Gass, I. A.; Batten, S. R.; Forsyth, C. M.; Moubaraki, B.; Schneider, C. J.; Murray, K. S. Supramolecular Aspects of Iron(II) Crown-Dipyridyl Spin-Crossover Compounds. *Coord. Chem. Rev.* **2011**, *255*, 2058–2067. (c) Roberts, T. D.; Tuna, F.; Malkin, T. L.; Kilner, C. A.; Halcrow, M. A. An Iron(II) Complex Exhibiting Five Anhydrous Phases, Two of Which Interconvert by Spin-Crossover with Wide Hysteresis. *Chem. Sci.* **2012**, *3*, 349–354. (d) Costa, J. S.; Rodríguez-Jménez, S.; Craig, G. A.; Barth, B.; Beavers, C. M.; Teat, S. J.; Aromí, G. Three-Way Crystal-to-Crystal Reversible Transformation and Controlled Spin Switching by a Nonporous Molecular Material. *J. Am. Chem. Soc.* **2014**, *136*, 3869–3874. (e) Phonsri, W.; Davies, C. G.; Jameson, G. N. L.; Moubaraki, B.; Murray, K. S. Spin Crossover, Polymorphism and Porosity to Liquid Solvent in Heteroleptic Iron(III) {Quinolylsalicylaldimine/Thiosemicarbazone-Salicylaldimine} Complexes. *Chem. Eur. J.* **2016**, *22*, 1322–1333. (f) Bartual-Murgui, C.; Codina, C.; Roubeau, O.; Aromí, G. A Sequential Method to Prepare Polymorphs and Solvatomorphs of $[\mathrm{Fe(1,3\text{-}bpp)_2}](\mathrm{ClO_4})_2\cdot n\mathrm{H_2O}$ (n = 0, 1, 2) with Varying Spin-Crossover Behaviour. *Chem. Eur. J.* **2016**, *22*, 12767–12776. (g) Shao, D.; Shi, L.; Shen, F.-X.; Wei, X.-Q.; Sato, O.; Wang, X.-Y. Reversible On–Off Switching of the Hysteretic Spin Crossover in a Cobalt(II) Complex via Crystal to Crystal Transformation. *Inorg. Chem.* **2019**, *58*, 11589–11598.

(45) (a) Hassan, N.; Koudriavtsev, A. B.; Linert, W. Isoequilibrium Relationships and Cooperative Effects in Spin-State Transitions in Solution. *Pure Appl. Chem.* **2008**, *80*, 1281–1292, (b) Barrett, S. A.; Kilner, C. A.; Halcrow, M. A. Spin-Crossover in $[\mathrm{Fe(3\text{-}bpp)_2}][\mathrm{BF_4}]_2$ in Different Solvents – a Dramatic Stabilisation of the Low-Spin State in Water. *Dalton Trans.* **2011**, *40*, 12021–12024.

(46) Fitting data in Figure 5 to eq 1 and 2 estimated $T_{½}$ = 446 ± 56 K for heterochiral $[\mathrm{Fe}((R)\text{-}L^1\mathrm{Ph})((S)\text{-}L^1\mathrm{Ph})][\mathrm{ClO_4}]_2$, and 414 ± 49 K for $[\mathrm{Fe}((R)\text{-}L^1i\mathrm{Pr})((S)\text{-}L^1i\mathrm{Pr})][\mathrm{ClO_4}]_2$.

(47) Kulmaczewski, R.; Howard, M. J.; Halcrow, M. A. Influence of Ligand Substituent Conformation on the Spin State of an Iron(II)/Di(pyrazol-1-yl)pyridine Complex. *Dalton Trans.* **2021**, *50*, 3464–3467.

(48) Houghton, B. J.; Deeth, R. J. Spin-State Energetics of Fe^{II} Complexes – the Continuing Voyage Through the Density Functional Minefield. *Eur. J. Inorg. Chem.* **2014**, *2014*, 4573–4580.

(49) Mortensen, S. R.; Kepp, K. P. Spin Propensities of Octahedral Complexes from Density Functional Theory. *J. Phys. Chem. A* **2015**, *119*, 4041–4050.

(50) The minimized low-spin Fe–N bond lengths are longer than the crystallographic values where the comparison can be made, by up to 1.6 % (or 8 crystallographic esds; Tables S10 and S11). Interestingly the greatest discrepancy is in low-spin $[\mathrm{Fe}(L^1\mathrm{H})_2]^{2+}$, which is not influenced by intramolecular steric interactions. As usual, the Fe–N distances in the high-spin minimizations deviate more strongly from experiment, by up to 2.7 %. In general, computed bond lengths in the $[\mathrm{Fe}(L^2\mathrm{R})_2]^{2+}$ series are closer to experiment than for $[\mathrm{Fe}(L^1\mathrm{R})_2]^{2+}$.

(51) Reiher, M.; Salomon, O.; Hess, B. A. Reparameterization of Hybrid Functionals Based on Energy Differences of States of Different Multiplicity. *Theor. Chem. Acc.* **2001**, *107*, 48–55.

(52) Zein, S.; Borshch, S. A.; Fleurat-Lessard, P.; Casida, M. E.; Chermette, H. Assessment of the Exchange-Correlation Functionals for the Physical Description of Spin Transition Phenomena by Density Functional Theory Methods: All the Same? *J. Chem. Phys.* **2007**, *126*, 014105.

(53) Deeth, R. J.; Halcrow, M. A.; Kershaw Cook, L. J.; Raithby, P. R. Ab Initio Ligand Field Molecular Mechanics and the Nature of Metal–Ligand π-Bonding in Fe(II) 2,6-Di(pyrazol-1-yl)pyridine Spin Crossover Complexes. *Chem. Eur. J.* **2018**, *24*, 5204–5212.

(54) Preliminary calculations were also attempted using another dispersion-corrected functional, PBE-D3. These also overstabilized the low-spin forms of $[\mathrm{Fe}(L^1\mathrm{R})_2]^{2+}$ and $[\mathrm{Fe}(L^2\mathrm{R})_2]^{2+}$ (R = Ph or *i*Pr), although the ΔE_{rel}\{HS-LS\} trends were closer to experiment than for B97-D2. The high-spin molecules often failed to minimize with PBE-D3, however, and the structures obtained were unrealistically distorted when R ≠ H. Hence, investigations with the PBE-D3 functional were discontinued.

(55) Ashley, D. C.; Jakubikova, E. Ironing Out the Photochemical and Spin-Crossover Behavior of Fe(II) Coordination Compounds with Computational Chemistry. *Coord. Chem. Rev.* **2017**, *337*, 97–111.

(56) (a) Jornet-Mollá, V.; Duan, Y.; Giménez-Saiz, C.; Tang, Y.-Y.; Li, P.-F.; Romero, F. M.; Xiong, R.-G. A Ferroelectric Iron(II) Spin Crossover Material. *Angew. Chem. Int. Ed.* **2017**, *56*, 14052–14056. (b) Akiyoshi, R.; Hirota, Y.; Kosumi, D.; Tsutsumi, M.; Nakamura, M.; Lindoy, L. F.; Hayami, S. Ferroelectric Metallomesogens Composed of Achiral Spin Crossover Molecules. *Chem. Sci.* **2019**, *10*, 5843–5848.

(57) Ohkoshi, S.; Takano, S.; Imoto, K.; Yoshikiyo, M.; Namai, A.; Tokoro, H. 90-Degree Optical Switching of Output Second-Harmonic Light in Chiral Photomagnet. *Nature Photon.* **2014**, *8*, 65–71.

(58) (a) Halcrow, M. A. Iron(II) Complexes of 2,6-Di(pyrazol-1-yl)pyridines – a Versatile System for Spin-Crossover Research. *Coord. Chem. Rev.* **2009**, *253*, 2493–2514. (b) Boča, M.; Jameson, R. F.; Linert. W. Fascinating variability in the chemistry and properties of 2,6-bis-(benzimidazol-2-yl)-pyridine and 2,6-bis-(benzthiazol-2-yl)-pyridine and their complexes. *Coord. Chem. Rev.* **2011**, *255*, 290–317. (c) Craig, G. A.; Roubeau, O.; Aromí, G. Spin State Switching in 2,6-Bis(pyrazol-3-yl)pyridine (3-bpp) Based Fe(II) Complexes. *Coord. Chem. Rev.* **2014**, *269*, 13–31.